Journal Pre-proof

Hard magnetics in ultra-soft magnetorheological elastomers enhance fracture toughness and delay crack propagation

Miguel Angel Moreno-Mateos, Mokarram Hossain, Paul Steinmann, Daniel Garcia-Gonzalez

Please cite this article as: M.A. Moreno-Mateos, M. Hossain, P. Steinmann et al., Hard magnetics in ultra-soft magnetorheological elastomers enhance fracture toughness and delay crack propagation. *Journal of the Mechanics and Physics of Solids* (2023), doi: https://doi.org/10.1016/j.jmps.2023.105232.

This is a PDF file of an article that has undergone enhancements after acceptance, such as the addition of a cover page and metadata, and formatting for readability, but it is not yet the definitive version of record. This version will undergo additional copyediting, typesetting and review before it is published in its final form, but we are providing this version to give early visibility of the article. Please note that, during the production process, errors may be discovered which could affect the content, and all legal disclaimers that apply to the journal pertain.

Hard magnetics in ultra-soft magnetorheological elastomers enhance fracture toughness and delay crack propagation

Miguel Angel Moreno-Mateos[a,*], Mokarram Hossain[b], Paul Steinmann[c,d], Daniel Garcia-Gonzalez[a,*]

[a]*Department of Continuum Mechanics and Structural Analysis, Universidad Carlos III de Madrid, Avda. de la Universidad 30, 28911 Leganés, Madrid, Spain*
[b]*Zienkiewicz Centre for Computational Engineering, Faculty of Science and Engineering, Swansea University, SA1 8EN, Swansea, UK*
[c]*Institute of Applied Mechanics, Universität Erlangen–Nürnberg, Egerland Str. 5, 91058 Erlangen, Germany*
[d]*Glasgow Computational Engineering Centre, School of Engineering, University of Glasgow, G12 8QQ, UK*

Abstract

Pre-existing flaws in highly stretchable elastomers trigger fracture under large deformations. For multifunctional materials, fracture mechanics may be influenced by additional physical phenomena. This work studies the implications of hard magnetics on the fracture behaviour of ultra-soft magnetorheological elastomers (MREs). We experimentally demonstrate that MREs with remanent magnetisation have up to a 50 % higher fracture toughness than non pre-magnetised samples. Moreover, we report crack closure due to the magnetic field as a mechanism that delays the opening of cracks in pre-magnetised MREs. To overcome experimental limitations and provide further understanding, a phase-field model for the fracture of MREs is conceptualised. The numerical model incorporates magneto-mechanical coupling to demonstrate that the stress concentration at the crack tip is smaller when the MRE is pre-magnetised. Overall, this work unveils intriguing applications for functional actuators, with better fracture behaviour and potential better performance under cyclic loading.

Keywords: Hard magnetics, Ultra-soft magnetorheological elastomers, Multifunctional materials, Experimental mechanics, Phase-field modelling, Soft fracture

*Corresponding authors

Email addresses: migmoren@ing.uc3m.es (Miguel Angel Moreno-Mateos), danigarc@ing.uc3m.es (Daniel Garcia-Gonzalez)

1. Introduction

Soft materials that respond to magnetic stimuli are able to modulate their material properties and change their shape in a remote and fast manner. Such features enable them for exciting applications in the bioengineering field such as intelligent substrates for cell stimulation (Moreno-Mateos et al., 2022a; Uslu et al., 2021) and soft robots for untethered navigation along biological tissues (Hu et al., 2018; Kim et al., 2019, 2018; Ren et al., 2019; Zhang et al., 2021; Wang et al., 2022b). In addition, high performance vibration absorbers (Li et al., 2022) and smart adhesives (Zhao et al., 2022) take advantage of the properties of these non-conventional materials. Composed of magnetic particles embedded in an elastomeric matrix, they are called magnetorheological elastomers (MREs). The stiffness of the matrix modulates both the magneto-mechanical stiffening and magnetostriction, i.e., material deformation under magnetic actuation (Garcia-Gonzalez et al., 2021; Silva et al., 2022; Pathak et al., 2022). In this regard, the use of ultra-soft elastomeric matrices enables significant actuation with small magnetic fields (Schümann and Odenbach, 2017; Moreno et al., 2021; Moreno-Mateos et al., 2022c,b; Lopez-Donaire et al., 2022).[1] When the magnetic particles are hard-magnetic, they allow for structures able to perform functional morphological changes, hereafter referred as hard-magnetic MREs (hMREs) (Kalina et al., 2017; Zhao et al., 2019; Wu et al., 2020; Moreno-Mateos et al., 2022c). Once the particles are permanently magnetised, they establish a remanent magnetic field even in the absence of an external magnetic actuation (Zhang and Rudykh, 2022; Stepanov et al., 2012). This enables for self-sustained magneto-mechanical improvement in terms of mechanical performance. Furthermore, under external magnetic actuation, the particles tend to rotate following the external magnetic field. The resulting transfer of torques to the soft matrix drives the shape morphing capability of these multifunctional structures (Moreno-Mateos et al., 2022b; Bastola and Hossain, 2021).

The fast growing of ultra-soft polymers is accompanied with the study of their failure mech-

---

[1]Note that we use the term "ultra-soft" to insist on the extremely soft nature of the matrix (below 10 kPa) in comparison to other conventional elastomers with stiffness several orders above. This term is used simply as an adjective to describe the nature of the MRE used. Therefore, this definition does not add any special consideration in the constitutive framework (rather than the use of finite deformation theory).

anisms. Recent applications, such as the development of skin patches based on soft polymers (Theocharidis et al., 2022), meshes for wound closure (Gao et al., 2021) and bioadhesive skin sensors (Wang et al., 2022a; Ma et al., 2022) require understanding fracture mechanisms in soft matter to design materials with improved fracture behaviour. A point of common interest concerns the strategies to enhance the fracture toughness, understood as the fracture energy density, of soft polymers (Zhao, 2017; Sanoja et al., 2021). To accomplish this, Lin and co-authors reported chain entanglement of the polymeric matrix as a potential mechanism (Lin et al., 2022). Moreover, time-delay in crack propagation is a factor that reduces fracture likelihood and benefits the design of such functional applications. In this regard, Li et. al (Li et al., 2021) reported mesoscale phase contrast with tough mesophase structures to design self-healing, tough and fatigue-resistant soft materials. Strategies to modify the crack path and fiber reinforced composites have also been reported to arrest crack propagation (Lee and Pharr, 2019; Li et al., 2020). Overall, the fracture performance of multifunctional materials is determined by their constitutive behaviour, which relies on an intricate coupling of several physical phenomena. For the case of hMREs, the structural response results from complex magneto-mechanical interactions at the microscale. Here, the interplay between the matrix and the magnetic particles affects the effective material parameters, e.g., the macroscopic mechanical stiffness. In this respect, the advancement of MREs poses a question on whether the magnetisation state may enhance the fracture behaviour of soft hMREs under large deformations. To the best of the authors' knowledge, there is still no work that studies the fracture behaviour of MREs, neither from the experimental nor from the computational point of view.

Although there are no studies on the fracture behaviour of MREs, their passive mechanical contribution to fracture is related to the soft polymeric matrix and the effect of the fillers. In this regard, strategies to elaborate on the fracture performance of highly stretchable polymers rely on experimental and computational approaches. Experimental methods comprise peeling and tack experiments on soft adhesives and fracture mechanics tests on films, sheets or thick polymeric samples (Akono et al., 2011; Creton and Ciccotti, 2016). While experimental tests mainly focus on a macroscopic viewpoint, *in silico* approaches provide further understanding of the underlying

3

physics of the problem and allow for the consideration of the microstructural composition (Swamy-
nathan et al., 2022). Here, the phase-field approach has been widely used in the last decade. In the
literature, the work by Miehe and co-authors (Miehe et al., 2010b) advocated a phase-field model
for fracture. Kumar et al. (Kumar et al., 2020) revisited the constitutive foundations accounting for
crack nucleation, Loew et al. (Loew et al., 2019) conceptualised a phase-field framework to model
the rate-dependent fracture of rubbers, Yu et al. (Yu et al., 2020) considered time-delayed fracture
due to solvent diffusion and Li et al. (Li et al., 2020) and Li et al. (Li et al., 2021) elaborated on
the fatigue resistance of soft elastomers and gels. Moreover, Ahmad et al. (Ahmad et al., 2020),
Zhou et al. (Zhou et al., 2021) and Chen et al. (Chen et al., 2017) studied the flaw-sensitivity
of highly stretchable polymers. This study is of great importance as pre-existing flaws are an un-
avoidable consequence from manufacturing processes and determine the fracture performance. In
addition, some authors have defined analytical expressions for the crack tip fields on highly stretch-
able elastomers (Begley et al., 2015; Long and Hui, 2015), which are useful for efficient analytical
approaches to the deformation problem and strain concentration of soft polymers. More recently,
Tan et al. (Tan et al., 2022) and Sridhar et al. (Sridhar and Keip, 2019) developed phase-field
models for multifunctional piezoelectric materials.

Here, based on a combination of experiments and theory, we uncover the fracture behaviour
of ultra-soft hMREs with remanent magnetic fields. For that, non-magnetised and pre-magnetised
hMRE samples with an ultra-soft elastomeric matrix ($\sim$ 1 kPa) are manufactured. Tensile tests
are used to demonstrate, for the first time in the literature, that remanent magnetic fields increase
the fracture toughness of pre-magnetised hMREs, i.e., the energy absorbed by the sample until
complete rupture (Chen et al., 2017; Zhou et al., 2021). Digital image correlation (DIC) allows to
calculate the strain fields at the crack tip and estimate the J-integral.[2] In addition, crack closure
due to the magnetic field is reported as a phenomenon that delays the opening of cracks. To pro-

---

[2]The Griffith approach identifies the energy release needed from the bulk to pay for the extra surface energy when
propagating a crack. In this regard, the J integral has the same interpretation, however the concept also carries over
to the large strain regime and the investment of the released energy can be done into any physical mechanism going
along with crack propagation, not only surface energy. Overall, our computation of J renders a quantity that is directly
related to the Griffith energy release.

vide further understanding into the constitutive basis of such a behaviour, this work conceptualises for the first time a bespoke numerical phase-field framework for fracture of hMREs. The results suggest that remanent magnetic fields induce beneficial compressive stresses in the medium as they decrease the stress concentration at the crack tip. Overall, we unveil intriguing potential applications for functional actuators with enhanced fracture performance and better behaviour under cyclic loading.

2. Methods

2.1. Materials and synthesis of the samples

The hMRE samples were manufactured from a blend of the elastomeric matrix and the magnetic particles. The matrix is an ultra-soft (≈ 1 kPa) PDMS, i.e., Dowsil CY52-276 (DowSil, Midland, MI, USA). It is composed of two phases that, when mixed in a 1:1 mass ratio, get cross-linked. The magnetic particles are NdFeB powder (MQP-S-11-9-grade powder, Neo Materials Technology Inc., Greenwood Village, Colorado, United States). They have hard-magnetic properties and a size of 25 - 55 μm. First, both phases of the matrix and the magnetic particles were mixed together and pre-heated at 85 ^{o}C for 2 min. The pre-heating initiates the crosslinking of the matrix and increases the initial viscosity of the mixture to prevent the sedimentation of the magnetic particles. Then, the moulds, also pre-heated, were filled with the blend to produce prismatic samples with 60 mm length, 10 mm width and 2 mm thickness. They were cured in the oven at 85 ^{o}C during 2 h. Hereafter, the following definition is important, i.e., non-magnetised samples as those without remanent magnetic field and pre-magnetised samples with remanent magnetic field. For pre-magnetised samples, an impulse magnetiser (DX-MAG20C, Dexing Magnet Tech. Co, Xiamen, China) applied permanent magnetisation in the longitudinal direction of the samples. The magnetiser was set at 1000 V, endowing the samples with an apparent macroscopic remanent magnetic induction of 40 mT (measured with a teslameter). Moreover, a blade was used to apply cuts on the samples of 1, 2, 3, 4, and 5 mm that define crack-width ratios of $c/w = 0.2, 0.3, 0.4, 0.5$, with c the length of the initial crack and w the width of the sample.

2.2. Experimental procedure for tensile tests

Quasi-static uniaxial tensile tests were performed with a universal testing machine (Instron 34TM-5, Norwood, Massachusetts, United States) at a velocity of 0.003 mm s^{-1}. The initial separation of the grips was set at $l_0 = 30$ mm and $l_0 = 50$ mm to get results for two different sample lengths. Special grips for ultra-soft polymers with pneumatic actuation were used. The tests finish when the sample breaks and the load falls to zero. In the mean while, force-displacement data was recorded. Supplementary Videos 1 and 2 show the deformation process for a non-magnetised and a pre-magnetised sample, respectively, with an initial cut of 5 mm.

2.3. Experimental procedure for digital image correlation

Pictures of the crack tip and surrounding area were taken during tensile tests. A CCD camera acquired images at a rate of 0.15 Hz, with resolution of 1032 x 772 pixels. The open source NCorr package, implemented in MatLab, was used to calculate the displacement fields and derive the Euler-Almansi strain fields. The resulting fields have a resolution of 0.05 mm/pixel. A subset with radius of 2.2 mm and spacing of 0.05 mm was chosen. To cope with large displacement, the correlation algorithm updates the reference image. Moreover, the analysis was done in a backwards manner to properly deal with the discontinuity of the crack. To this end, the final deformed image was taken as the reference one, and the correlations of all the others with smaller deformation were done with respect to that one.

2.4. Experimental estimation of J-integral

The J-integral is estimated from the displacement fields obtained with DIC and the analytical description of Long et al. (Long and Hui, 2015) for the crack tip fields under large deformations. The analytical approach is based on the Generalized neo-Hookean model (GNH) to fit the vertical displacement fields. The parameters of the GNH model were independently calibrated from tensile tests on non-magnetised and pre-magnetised hMRE specimens without initial cuts. For non-magnetised and pre-magnetised samples, respectively, shear moduli G of 6.2 kPa and 11 kPa and strain-hardening exponents n of 1.18 and 1.10 were calibrated (see Figure A.5). An annular grid places the fitting points far enough from the crack tip to avoid the dissipative length scale,

6

and far enough from the boundary to avoid boundary effects (Long et al., 2021; Vasco-Olmo et al., 2015).

The analytical model relies on the method of asymptotic analysis and the Generalised neo-Hookean Model (GNH). Stephenson (Stephenson, 1982) established that the elastic potential near the crack tip is governed by

$$\Psi = AI_1^n + BI_1^{n-1}, \tag{1}$$

with A, B and n material parameters and $I_1 = \text{tr}\,(\mathbf{C})$, where $\mathbf{C} = \mathbf{F}^{\text{T}} \cdot \mathbf{F}$ with $\mathbf{F}$ the deformation gradient.

Analytically, the vertical displacement field is described by

$$u_2 = ar^{1-\frac{1}{2n}}U(\theta, n), \tag{2}$$

with a an amplitude parameter, r the radial coordinate with respect to crack tip and $U(\theta, n)$ an odd function of the angular coordinate θ, defined as

$$U(\theta, n) = \sin(\theta/2)\sqrt{1 - \frac{2\kappa^2 \cos^2(\theta/2)}{1 + \omega(\theta, n)}} \left[\omega(\theta, n) + \kappa\cos(\theta)\right]^{\kappa/2}, \tag{3}$$

with

$$\kappa = 1 - \frac{1}{n}, \quad \omega(\theta, n) = \sqrt{1 - \kappa^2 \sin^2(\theta)}. \tag{4}$$

Finally, the amplitude parameter a, hence the displacement field u_2, is related to J according to

$$J = \frac{G\pi}{2}\left[\frac{b}{n}\right]^{n-1}\left[\frac{2n-1}{2n}\right]^{2n-1} n^{1-n}a^{2n}. \tag{5}$$

with G the shear modulus and b a material parameter of the GNH model. Detail on the calibration of these parameters is provided in Appendix A.

The fitting with the experimental and analytical displacement field is done at the i points defined by the annular grid in Figure 3.e.1, by taking J as unknown variable, and performing least squares

7

fitting, according to

$$\min_{J \in \mathbb{R}^+} \sum_i^n \left[u_{2,theo}^{2n} - u_{2,exp}^{2n} \right]_i^2. \tag{6}$$

2.5. Constitutive framework for fracture of hard-magnetic magnetorheological elastomers

The deformation of the ultra-soft hard-magnetic MRE (hMRE) is formulated in a finite strain framework. A function $\mathbf{x} = \boldsymbol{\varphi}(\mathbf{X})$ maps the coordinates in the undeformed or material configuration $\mathbf{X} \in \Omega_0$ to the coordinates in the deformed or spatial configuration $\mathbf{x} \in \Omega$. The external boundary is denoted by $\partial \Omega_0$ in the material configuration and $\partial \Omega$ in the spatial configuration. The displacement field, i.e., the unknown field of the mechanical problem, is $\mathbf{u} = \boldsymbol{\varphi}(\mathbf{X}) - \mathbf{X}$. The deformation gradient is defined as

$$\mathbf{F} = \boldsymbol{\nabla}_0 \boldsymbol{\varphi} = \boldsymbol{\nabla}_0 \mathbf{u} + \mathbf{I}, \tag{7}$$

where $\boldsymbol{\nabla}_0$ is the gradient with respect to the material configuration and $\mathbf{I}$ the second-order identity tensor.

The magnetic problem is formulated on a primary scalar potential field ϕ. The magnetic field vector $\mathbb{H}$ is defined as

$$\mathbb{H} = -\boldsymbol{\nabla}_0 \phi = \mathbb{H}_e + \mathbb{H}_r. \tag{8}$$

The magnetic field is split into an energetic contribution $\mathbb{H}_e$ due to the magnetic susceptibility of the medium and a remanent contribution $\mathbb{H}_r$ related to the permanent magnetisation of the hMRE (Mukherjee et al., 2021). The last one is prescribed as a constant vector to capture the permanent magnetisation of the medium following a previous work by the authors (Moreno-Mateos et al., 2022b). The experimental measure of the apparent (homogeneous) magnetic induction of a pre-magnetised hMRE with a teslameter provides a value of $\mathbb{H}_r = 20$ mT.

Finally, the damage field d is a scalar order parameter that describes whether a continuum point is damaged or not. This non-local strategy allows to model crack growth and the consequent degradation of the properties on damaged areas. As reported by Kumar and co-authors (Kumar et al., 2020), compressibility of the medium is paramount to avoid non physical behaviour. A

8

non-local field equation governs the evolution of damage. To this end, the crack surface energy is regularized and transformed to a volumetric energy. Thereby, the continuous crack surface density function per unit volume is defined according to Ambrosio et al. (Ambrosio and Tortorelli, 1992) as

$$\gamma\left(d, \boldsymbol{\nabla} d\right) = \frac{3}{8}\left[\frac{d}{l} + l|\boldsymbol{\nabla} d|^2\right],\tag{9}$$

with $\boldsymbol{\nabla} = \boldsymbol{\nabla}_0 \cdot \mathbf{F}^{-1}$ the gradient with respect to the spatial configuration. Note that Eq. 9 considers d as alternative to d^2 as often used alternatively.[3]

Furthermore, we define $g_1\left(d\right)$ as degradation function

$$g_1\left(d\right) = \left[1 - d\right]^2.\tag{10}$$

Note that this second order function is a free constitutive choice. Alternative mathematical functions could also be implemented and tested.

The constitutive formulation is based on an additive decomposition of the total energy density into mechanical, Maxwell (i.e., magnetic vacuum), matter magnetisation and magneto-mechanical coupling contributions as

$$\Psi\left(\mathbf{F}, \mathbb{H}\right) = g_2\left(d\right)\Psi_{\text{mech}}\left(\mathbf{F}\right) + \Psi_{\text{maxw}}\left(\mathbf{F}, \mathbb{H}\right) + g_1\left(d\right)\Psi_{\text{mag}}\left(\mathbf{F}, \mathbb{H}\right) + g_1\left(d\right)\Psi_{\text{coup}}\left(\mathbf{F}, \mathbb{H}\right).\tag{11}$$

The degradation of all the components except for the Maxwell one guarantees the continuity of the magnetic problem as fully damaged domains are treated as air (i.e., vacuum magnetic properties). Note that we define a second degradation function as $g_2\left(d\right) = \left[\left[1 - d\right]^2 + k\right]$, which is essentially the same as $g_1\left(d\right)$, but incorporates a parameter $k = 1 \cdot 10^{-3}$ to introduce a residual mechanical stiffness on damaged areas and ensure numerical convergence (Miehe et al., 2010a).

---

[3]There exist two common options for the definition of the crack surface density function (Ambrosio and Tortorelli, 1992; Kumar et al., 2018a; Hirshikesh et al., 2019; Vicentini et al., 2023; Lo et al., 2022), i.e., AT1: $\gamma\left(d, \boldsymbol{\nabla} d\right) = \frac{3}{8}\left[\frac{d}{l} + l|\boldsymbol{\nabla} d|^2\right]$ and AT2: $\gamma\left(d, \boldsymbol{\nabla} d\right) = \frac{1}{2}\left[\frac{d^2}{l} + l|\boldsymbol{\nabla} d|^2\right]$. Throughout this work we focus on the AT1 model.

9

The total rate potential functional of the solid is

$$\dot{\Pi} = \dot{\Pi}_{\text{int}} + \dot{D}_{\text{crack}} + \dot{D}_{\text{crack,visc}} - \dot{\Pi}_{\text{ext}}, \tag{12}$$

Therein, the internal power is

$$\dot{\Pi}_{\text{int}} = \int_{\Omega_0} \left[\partial_{\mathbf{F}} \, \Psi : \dot{\mathbf{F}} + \partial_{\mathbb{H}} \, \Psi \cdot \dot{\mathbb{H}} + \Psi_{\text{mat}} \partial_d \, g_1 \dot{d} \right] dV, \tag{13}$$

with $\Psi_{\text{mat}} = \Psi_{\text{mech}} + \Psi_{\text{mag}} + \Psi_{\text{coup}}$ the material energy density.

The dissipation rate potential functional due to crack formation $\dot{D}_{\text{crack}}$ is

$$\dot{D}_{\text{crack}} = \int_{\Omega} G_{\text{c}} \dot{\gamma} \, dV = \int_{\Omega} \frac{3G_{\text{c}}}{8} \left[\frac{\dot{d}}{l} + 2l \boldsymbol{\nabla} d \boldsymbol{\nabla} \dot{d} \right] dV, \tag{14}$$

the rate-dependent crack growth dissipation potential $\dot{D}_{\text{crack,visc}}$ is as in (Loew et al., 2019; Miehe and Schänzel, 2014)

$$\dot{D}_{\text{crack,visc}} = \int_{\Omega} \frac{\eta}{2} \dot{d}^2 \, dV, \tag{15}$$

and the external power $\dot{\Pi}_{\text{ext}}$ reads

$$\dot{\Pi}_{\text{ext}} = \int_{\Omega_0} \mathbf{b}_0 \cdot \dot{\mathbf{u}} \, dV + \int_{\partial\Omega_0} \mathbf{t}_0 \cdot \dot{\mathbf{u}} \, dA, \tag{16}$$

with $\mathbf{b}_0$ and $\mathbf{t}_0$ the body and traction force vectors, respectively, in the material configuration.

The fracture parameters are the critical energy release rate $G_c = 4.9 \cdot 10^{-2} \, \frac{\text{N}}{\text{mm}}$ and the length scale parameter $l = 0.1$ mm (see Figure 3 for the calibration of G_{c}). The latter is chosen small enough with respect to the dimensions of the sample. In addition, the viscosity parameter $\eta = 0.1$ allows for the rate dependent formation of cracks. In this work it is used as a numerical viscous regularisation and to improve the robustness of the numerical results.

10

From the rate potential, an incremental potential can be integrated as

$$\Pi = \int_{t}^{t+\Delta t} \dot{\Pi}\, \mathrm{d}t. \tag{17}$$

The optimization of the potential[4] in Eq. 17 with respect to d, or alternatively the variation of the rate potential in Eq. 12 with respect to $\dot{d}$, yields the local phase-field equation. Recent works 200 have studied the implications of pre-existing flaws and material strength (Kumar et al., 2018b,a). To reconcile crack nucleation with the current approaches and keep the characteristic length l as a regularisation parameter independent of the strength, an amended form of the phase-field equation incorporates an additional configurational force c_{e}. It reads as

$$\frac{\partial \overline{\Pi}}{\partial d} = \frac{3G_c}{8}\left[\frac{1}{l} - 2l\boldsymbol{\nabla}^2 d\right] + g_1'(d)\,\Psi_{\mathrm{mat}}^+ + \eta\dot{d} + c_{\mathrm{e}} = 0, \tag{18}$$

where $g_1'(d)$ is the derivative with respect to the damage field. The thermodynamic consistency of 205 the model is guaranteed when the viscous resistance term $\eta\dot{d} \geq 0$, i.e., $\dot{d} \geq 0$ and $\eta \geq 0$.

The configurational external force c_{e} has been included following (Kumar et al., 2018b,a) to account for the hydrostatic strength of the material. It reads as

$$c_{\mathrm{e}} = -\left[1 - d\right]\frac{3^{5/4}G_{\mathrm{c}}\kappa}{2l\sigma_{\mathrm{hs}}}\frac{\mathrm{tr}\,(\mathbf{H})}{\left[3 + \mathbf{H} : \mathbf{H}\right]^{5/4}}, \tag{19}$$

with $\mathbf{H} = \mathbf{F} - \mathbf{I}$, κ the bulk modulus and $\sigma_{\mathrm{hs}} = \frac{1}{3}\mathrm{tr}\,(\boldsymbol{\sigma}_{\mathrm{s}}) = 0.065$ MPa the spherical critical stress, determined from a tensile test to rupture of a bulk (i.e., uncut) hMRE sample (see Figure A.5).

210 In Eq. 18 the positive energy density Ψ_{mat}^+ is defined with the magnetic contribution that induces

---

[4]Without loss of consistency, the governing equation for the phase-field problem derives from an amended internal potential $\overline{\Pi}_{\mathrm{int}}$. This potential differs from Π_{int} in the effective energetic material contribution. In this regard, we define an amended material energy Ψ_{mat}^+ because expansive magnetic volumetric contributions lead to mechanical compression of the MRE. Therefore, only compressive contributions should favour material damage.

11

the expansion of the medium as

$$
\Psi_{\text{mat}}^{+} =
\begin{cases}
\Psi_{\text{mech}}, & \text{if } \alpha \geq 0 \\
\Psi_{\text{mech}} + \Psi_{\text{mag}} + \Psi_{\text{coup}}, & \text{if } \alpha < 0
\end{cases}
\tag{20}
$$

where $\alpha = \frac{1}{3}\text{tr}\left(\boldsymbol{\sigma}_{\text{mag}} + \boldsymbol{\sigma}_{\text{coup}} + \boldsymbol{\sigma}_{\text{maxw}}\right)$ is the spherical component of the magnetic Cauchy stress tensor. Figure D.8 shows the α field for different stages along the propagation of the crack. Note that we define Eq. 20 since expansive magnetic volumetric contributions lead to mechanical com-

215 pression of the hMRE. Therefore, only compressive contributions should favour material damage.

Moreover, to include the constraint $0 \leq d \leq 1$, penalty energy functions are included to the potential energy as

$$
\Pi_{\text{penalty}} =
\begin{cases}
10^4 G_c d^2, & \text{if } d < 0 \\
10^4 G_c \left[d - 1\right]^2, & \text{if } d > 1
\end{cases}
\tag{21}
$$

The optimization of Eq. 17 with respect to the primary field $\mathbf{u}$ and in the absence of body forces yields the mechanical field equation

$$
\frac{\partial \Pi}{\partial \mathbf{u}} = \boldsymbol{\nabla}_0 \cdot \mathbf{P} = \mathbf{0}.
\tag{22}
$$

220 Finally, the optimization of the potential in Eq. 17 with respect to the primary field ϕ yields the magnetic field equation, i.e., Maxwell's equation for the magnetic induction

$$
\frac{\partial \Pi}{\partial \phi} = -\boldsymbol{\nabla}_0 \cdot \mathbb{B} = 0.
\tag{23}
$$

The magnetic induction $\mathbb{B}$, magnetic field $\mathbb{H}$ and magnetisation $\mathbb{M}$, satisfy the following standard constitutive relation

$$
\mathbb{B} = J\mu_0 \mathbf{C}^{-1}\left[\mathbb{H} + \mathbb{M}\right],
\tag{24}
$$

with $\mathbf{C} = \mathbf{F}^{\text{T}} \cdot \mathbf{F}$ the right Cauchy-Green deformation tensor, μ_0 the magnetic permeability of
225 vacuum and $J = \det\left(\mathbf{F}\right)$ the Jacobian of the deformation gradient.

The constitutive formulation is based on the additive decomposition of the total energy density

12

in Eq. 11. The mechanical contribution consists in two parts: isochoric and volumetric energy densities $\Psi_{\text{mech,iso}}$ and $\Psi_{\text{mech,vol}}$, respectively. For the isochoric one, the Generalised neo-Hookean (GNH) model is chosen

$$\Psi_{\text{mech,iso}}\left(\mathbf{F}\right) = \frac{G}{2b}\left[\left[1 + \frac{b}{n}\left[I_1 - 3\right]\right]^n - 1\right], \tag{25}$$

with $I_1 = \text{tr}\left(\mathbf{F} \cdot \mathbf{F}^{\text{T}}\right)$ and G the small strain shear modulus of the considered phase and b and n material parameters. For the hMRE, $G = 6.2$ kPa, $b = 1$ and $n = 1.18$ according to the calibration in Appendix A from tests on non-magnetised samples.[5] For the air, modelled as an extremely compliant domain (Moreno-Mateos et al., 2022b), $G = 0.01$ kPa, $b = 1$ and $n = 1.18$.

The volumetric contribution is taken from (Miehe and Schänzel, 2014) as

$$\Psi_{\text{mech,vol}}\left(\mathbf{F}\right) = \frac{G}{\beta}\left[J^{-\beta} - 1\right], \tag{26}$$

with $\beta = \frac{2\nu}{1-2\nu}$ and ν the Poisson's ratio. To allow larger deformation of the damaged material, we have followed an approach similar to the one reported by Li et al. (Li and Bouklas, 2020) where the bulk modulus is degraded faster than the shear modulus. We make ν depend on the damage variable $\nu\left(d\right) = \left[1 - d^2\right]\nu_1 + \left[1 - \left[1 - d\right]^2\right]\nu_2$, with $\nu_1 = 0.47$ the material Poisson's ratio and $\nu_2 = 0.2\,\nu_1$ a degraded Poisson's ratio. The Poisson's ratio of the air is set to $\nu_{\text{air}} = 0.4$.

The magnetic Maxwell energy describes the background magnetic energy due to the non-zero magnetic permeability of the vacuum as

$$\Psi_{\text{maxw}}\left(\mathbf{F}, \mathbb{H}\right) = -\frac{\mu_0}{2}JI_5^{\text{e}}, \tag{27}$$

with the energetic magnetic invariant $I_5^{\text{e}} = \left[\mathbf{F}^{-\text{T}} \cdot \mathbb{H}\right] \cdot \left[\mathbf{F}^{-\text{T}} \cdot \mathbb{H}\right]$.

The magnetic contribution is additively decomposed into an energetic term $\Psi_{\text{mag,e}}$ and a rema-

---

[5]Note that the mechanical contribution in the numerical model is calibrated from experimental results for tensile tests on non-magnetised samples and the magnetic fields for the pre-magnetisation condition are included through a magnetic constitutive extension of the model. This differs from the material parameters used for the estimation of the J-integral, where the GNH parameters are calibrated to include the magneto-rheological effect.

nent contribution $\Psi_{\text{mag,r}}$ as

$$\Psi_{\text{mag}}\left(\mathbf{F}, \mathbb{H}\right) = \Psi_{\text{mag,e}} + \Psi_{\text{mag,r}} = -\frac{\mu_0}{2} J \chi_{\text{e}} I_5^{\text{e}} + \mu_0 J \left[1 + \chi_{\text{e}}\right] I_5^{\text{er}} + \frac{\mu_0}{2\chi_{\text{r}}} J I_5^{\text{r}}, \tag{28}$$

245 where χ_{e} and χ_{r} are the energetic and remanent magnetic susceptibility, respectively, as in (Mukherjee et al., 2021). In the simulations, the remanent magnetic field is assumed to be constant. Therefore, the parameter χ_{r} does not affect the results.

The invariant $I_5^{\text{er}} = \mathbb{h} \cdot \mathbb{h}_{\text{r}} = \mathbb{H} \cdot \mathbf{C}^{-1/2} \cdot \mathbb{H}_{\text{r}}$ is uncoupled to the displacement field and accounts for the energetic and remanent magnetic fields in the Eulerian configuration of the medium.

250 An additional coupling term is included to account for the effect of the microstructural attraction forces between the particles, as reported in (Mukherjee et al., 2021)

$$\Psi_{\text{coup}} = \beta_{\text{coup}} \mu_0 J \left[\left[I_4^{\text{r}} - I_5^{\text{r}}\right] - 2\chi_{\text{e}} \left[I_4^{\text{er}} - I_5^{\text{er}}\right]\right], \tag{29}$$

with the coupled invariants $I_4^{\text{r}} = \mathbb{H}_{\text{r}} \cdot \mathbf{C} \cdot \mathbb{H}_{\text{r}}$ and $I_4^{\text{er}} = \mathbb{H} \cdot \mathbf{C}^{1/2} \cdot \mathbb{H}_{\text{r}}$, and the uncoupled invariant $I_5^{\text{r}} = \mathbb{H}_{\text{r}} \cdot \mathbb{H}_{\text{r}}$. The coupling parameter was calibrated from the experimental results on a uncut premagnetised sample, whereby it was reduced to $\beta_{\text{coup}} = 1$ to guarantee the numerical stability of 255 the problem. Despite this consideration, and without loss of generality, the numerical framework faithfully solves the actual physics of the fracture problem. It reproduces the same tendencies that are observed experimentally and it allows to explore the magneto-mechanical stress fields around the crack tip.

The total Piola stress is derived from the total energy potential in Eq. 11 according to

$$\mathbf{P}\left(\mathbf{F}, \mathbb{H}\right) = \frac{\partial \Psi}{\partial \mathbf{F}} = g_2 \mathbf{P}_{\text{mech,iso}} + g_2 \mathbf{P}_{\text{mech,vol}} + \mathbf{P}_{\text{maxw}} + g_1 \mathbf{P}_{\text{mag,e}} + g_1 \mathbf{P}_{\text{mag,r}} + g_1 \mathbf{P}_{\text{coup}} = \tag{30}$$
$$= g_2 G \mathbf{F} \left[1 + \frac{b}{n} \left[I_1 - 3\right]\right]^{n-1} - g_2 G J^{-\beta} \mathbf{F}^{-\text{T}} - \frac{1}{2} \mu_0 J \frac{\partial I_5^{\text{e}}}{\partial \mathbf{F}} - g_1 \frac{1}{2} \mu_0 J \chi_{\text{e}} \frac{\partial I_5^{\text{e}}}{\partial \mathbf{F}}$$
$$+ g_1 \mu_0 J \left[1 + \chi_{\text{e}}\right] \frac{\partial I_5^{\text{er}}}{\partial \mathbf{C}} : \frac{\partial \mathbf{C}}{\partial \mathbf{F}} + g_1 \mu_0 \beta_{\text{coup}} J \left[\mathbb{H}_{\text{r}} : \frac{\partial \mathbf{C}}{\partial \mathbf{F}} : \mathbb{H}_{\text{r}} - 2\chi_{\text{e}} \left[\frac{\partial I_4^{\text{er}}}{\partial \mathbf{F}} - \frac{\partial I_5^{\text{er}}}{\partial \mathbf{F}}\right]\right],$$

14

with the derivative of the invariant I_5^{e}

$$\frac{\partial I_5^{\mathrm{e}}}{\partial \mathbf{F}} = -2 \left[\mathbf{F}^{-\mathrm{T}} \cdot \mathbb{H}\right] \otimes \left[\left[\mathbb{H} \cdot \mathbf{F}^{-1}\right] \cdot \mathbf{F}^{-\mathrm{T}}\right]. \tag{31}$$

260 The derivative of I_4^{er} is taken from (Mukherjee et al., 2021)

$$\frac{\partial I_4^{\mathrm{er}}}{\partial \mathbf{C}} = \frac{4}{\Delta}\Big[I_1^{\mathrm{U}} \mathbf{C}\, \mathrm{sym}\,(\mathbb{H} \otimes \mathbb{H}_{\mathrm{r}})\, \mathbf{C} - \left(I_1^{\mathrm{U}}\right)^2 \left[\mathbf{C}\, \mathrm{sym}\,(\mathbb{H} \otimes \mathbb{H}_{\mathrm{r}})\, \mathbf{C}^{1/2} + \mathbf{C}^{1/2} \mathrm{sym}\,(\mathbb{H} \otimes \mathbb{H}_{\mathrm{r}})\, \mathbf{C}\right] +$$
$$\left[I_1^{\mathrm{U}} I_2^{\mathrm{U}} - I_3^{\mathrm{U}}\right] \left[\mathbf{C}\, \mathrm{sym}\,(\mathbb{H} \otimes \mathbb{H}_{\mathrm{r}}) + \mathrm{sym}\,(\mathbb{H} \otimes \mathbb{H}_{\mathrm{r}})\, \mathbf{C}\right] + \left[\left(I_1^{\mathrm{U}}\right)^3 + I_3^{\mathrm{U}}\right] \mathbf{C}^{1/2}\, \mathrm{sym}\,(\mathbb{H} \otimes \mathbb{H}_{\mathrm{r}})\, \mathbf{C}^{1/2} -$$
$$\left(I_1^{\mathrm{U}}\right)^2 I_2^{\mathrm{U}} \left[\mathbf{C}^{1/2} \mathrm{sym}\,(\mathbb{H} \otimes \mathbb{H}_{\mathrm{r}}) + \mathrm{sym}\,(\mathbb{H} \otimes \mathbb{H}_{\mathrm{r}})\, \mathbf{C}^{1/2}\right] +$$
$$\left[\left(I_1^{\mathrm{U}}\right)^2 I_3^{\mathrm{U}} + \left[I_1^{\mathrm{U}} I_2^{\mathrm{U}} - I_3^{\mathrm{U}}\right] I_2^{\mathrm{U}}\right] \mathrm{sym}\,(\mathbb{H} \otimes \mathbb{H}_{\mathrm{r}})\Big], \tag{32}$$

with $\Delta = 8 \left[I_1^{\mathrm{U}} I_2^{\mathrm{U}} - I_3^{\mathrm{U}}\right] I_3^{\mathrm{U}}$. Note that I_1^{U}, I_2^{U} and I_3^{U} are the three principal invariants of $\mathbf{U} = \mathbf{C}^{1/2}$. Similarly, the derivative of I_4^{er} is

$$\frac{\partial I_5^{\mathrm{er}}}{\partial \mathbf{C}} = -\frac{4}{\Delta}\Big[I_1^{\mathrm{U}} \mathbf{C}^{1/2}\, \mathrm{sym}\,(\mathbb{H} \otimes \mathbb{H}_{\mathrm{r}})\, \mathbf{C}^{1/2} - \left(I_1^{\mathrm{U}}\right)^2 \left[\mathbf{C}^{1/2}\, \mathrm{sym}\,(\mathbb{H} \otimes \mathbb{H}_{\mathrm{r}}) + \mathrm{sym}\,(\mathbb{H} \otimes \mathbb{H}_{\mathrm{r}})\, \mathbf{C}^{1/2}\right] +$$
$$\left[I_1^{\mathrm{U}} I_2^{\mathrm{U}} - I_3^{\mathrm{U}}\right] \left[\mathbf{C}^{1/2}\, \mathrm{sym}\,(\mathbb{H} \otimes \mathbb{H}_{\mathrm{r}})\, \mathbf{C}^{-1/2} + \mathbf{C}^{-1/2}\, \mathrm{sym}\,(\mathbb{H} \otimes \mathbb{H}_{\mathrm{r}})\, \mathbf{C}^{1/2}\right] + \left[\left(I_1^{\mathrm{U}}\right)^3 + I_3^{\mathrm{U}}\right] \mathrm{sym}\,(\mathbb{H} \otimes \mathbb{H}_{\mathrm{r}}) -$$
$$\left(I_1^{\mathrm{U}}\right)^2 I_2^{\mathrm{U}} \left[\mathrm{sym}\,(\mathbb{H} \otimes \mathbb{H}_{\mathrm{r}})\, \mathbf{C}^{-1/2} + \mathbf{C}^{-1/2}\, \mathrm{sym}\,(\mathbb{H} \otimes \mathbb{H}_{\mathrm{r}})\right] +$$
$$\left[\left(I_1^{\mathrm{U}}\right)^2 I_3^{\mathrm{U}} + \left[I_1^{\mathrm{U}} I_2^{\mathrm{U}} - I_3^{\mathrm{U}}\right] I_2^{\mathrm{U}}\right] \mathbf{C}^{-1/2}\, \mathrm{sym}\,(\mathbb{H} \otimes \mathbb{H}_{\mathrm{r}})\, \mathbf{C}^{-1/2}\Big]. \tag{33}$$

Likewise, the magnetic induction is obtained from the energy density function through constitutive arguments as

$$\mathbb{B}\,(\mathbf{F}, \mathbb{H}) = -\frac{\partial \Psi}{\partial \mathbb{H}} = \mathbb{B}_{\mathrm{maxw}} + g_1 \mathbb{B}_{\mathrm{mag,e}} + g_1 \mathbb{B}_{\mathrm{mag,r}} + g_1 \mathbb{B}_{\mathrm{coup}} = \tag{34}$$
$$= \mu_0 J \mathbf{F}^{-1} \cdot \mathbf{F}^{-\mathrm{T}} \cdot \mathbb{H} + g_1 \mu_0 J \chi_{\mathrm{e}} \mathbf{F}^{-1} \cdot \mathbf{F}^{-\mathrm{T}} \cdot \mathbb{H} - g_1 \mu_0 J \left[1 + \chi_{\mathrm{e}}\right] \mathbb{H}_{\mathrm{r}} \cdot \mathbf{C}^{-1/2}$$
$$- g_1 2 \mu_0 \beta_{\mathrm{coup}} J \chi_{\mathrm{e}} \left[\mathbf{C}^{-1/2} - \mathbf{C}^{1/2}\right] \cdot \mathbb{H}_{\mathrm{r}}.$$

The first variation of the field equations (mechanical, magnetic and damage field equations)

15

yields the weak form of the problem, which is numerically solved in the open source finite element

265 environment FEniCS using the NonLinearVariationalProblem library (Logg et al., 2012). The magneto-mechanical problem and the phase-field problem are decoupled in a staggered scheme and the magneto-mechanical problem is solved monolithically. Iterations stop when the maximum difference of the fields between two consecutive iterations is smaller than a tolerance, here set to $tol_1 = 1 \cdot 10^{-2}$. This approach ensures computational efficiency and is more robust than the

270 monolithic problem (Miehe et al., 2010b). However, the staggered scheme requires small enough load steps. To decrease the calculation time, we implement an adaptive load stepping that increases and reduces the load step according to the growth of the damage variable (Loew et al., 2019). For an increase larger than $tol_2 = 0.15$, the load increment is reduced by a factor of $1/1.2$ up to a minimum value of $\Delta_t = 1 \cdot 10^{-3}$. Otherwise, it is incremented by a factor of 1.2 up to a maximum

275 value of $\Delta_t = 1.6 \cdot 10^{-2}$.

The finite element computation was performed on a two-dimensional mesh. Although this consideration disregards the finite thickness of the MRE samples, the simplification is necessary to pose a computationally resolvable model while keeping the mesh fine enough within the crack region. The boundaries of the air sub-domain were mechanically fixed with null perpendicular

280 displacements. Moreover, multipoint constraints were applied on the displacement field of the air to enhance the numerical convergence. To mimic a tensile test, the displacement of the upper and lower edges of the rectangular sample are constrained. A first stage allows for the pre-compression of the sample with the application of the remanent magnetic field. A second stage applies vertical displacements of the edges. With regard to the magnetic field, the magnetic potential was set to zero

285 on a reference point and the background Maxwell stress contribution was subtracted from the stress as it is balanced by the stress from the surrounding air. Finally, initial damage representing the pre-existing crack is prescribed directly on the phase-field as $d = 1$. In addition, the contribution to the weak form due to the phase-field equation is restricted to the sub-domain of the hMRE. To this end, the contribution of the air is excluded from the residual and the phase-field is set to zero in the

290 air.

16

2.6. Treatment of the air domain: multipoint constraints

The air (free space) is modelled as a compliant sub-domain that surrounds the hMRE and deforms with it (Moreno-Mateos et al., 2022b). To avoid interpenetration of the elements on the upper and lower edges of the hMRE sample, multipoint constraints prescribe the vertical displacement field on the regions of the air above and below the sample, see Figure 1 (Rambausek et al., 2022; Mukherjee and Danas, 2022). A second-order polynomial is defined to be $u_{2,\mathrm{hMRE}}$ (i.e., vertical displacement of the upper and lower edges of the hMRE sample) in the middle horizontal coordinate and zero on the left and right boundaries, and a first-order polynomial is defined to be $u_{2,\mathrm{hMRE}}$ in the upper and lower edges of the hMRE sample and zero in the top and bottom boundaries.
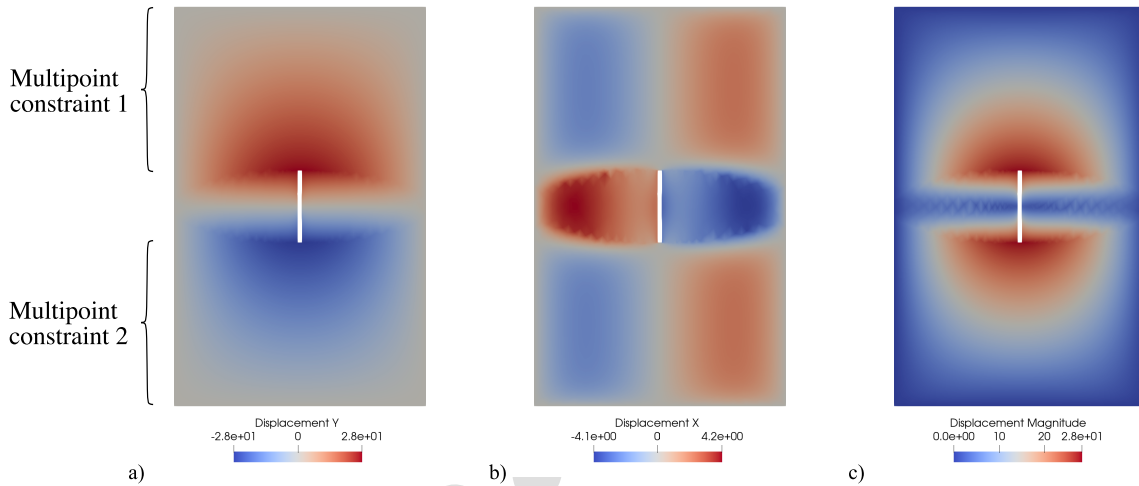
Figure 1. **Multipoint constraints on the vertical displacement fields of the air sub-domain to improve numerical stability.** A second-order polynomial is defined to be $u_{2,\mathrm{hMRE}}$ in the middle horizontal coordinate and zero on the left and right boundaries, and a first-order polynomial is defined to be $u_{2,\mathrm{hMRE}}$ in the upper and lower edges of the sample and zero in the top and bottom boundaries. (a) Vertical displacement field of the air sub-domain, (b) horizontal displacement field and (c) magnitude of the displacement field.

3. Results

3.1. Hard magnetics improve fracture toughness of hMREs

The constitutive behaviour of MREs is highly influenced by the interaction between the magnetic particles, the soft matrix, and the external magnetic field. When MREs are manufactured with hard-magnetic particles, magneto-mechanical effects (e.g., structural stiffening) can be sustained even in the absence of magnetic fields. These premises suggest that also their fracture

17

behaviour must depend on the microstructural magneto-mechanical coupling. To elaborate on this hypothesis, we manufacture non-magnetised hMRE samples (without remanent magnetic field) and pre-magnetised samples (with remanent magnetic field). To unveil the dependence on the size of pre-existing flaws, cuts of different sizes are applied, i.e., from 1 mm to 5 mm. The rectangular samples, with length, width and thickness of 30/50 mm, 10 mm and 2 mm, respectively, are tested under tensile loading until fracture. Details on the experimental procedure can be found in Methods 2.2. Moreover, Figure 2.b illustrates the geometry of the samples.

The force-displacement curves in Figure 2.a are used to calculate the fracture energy density, i.e., a measure of the fracture toughness (Chen et al., 2017), as the area under the curves divided by the volume of the samples. The results permit to compare the fracture toughness of hMREs with different cut lengths and remanent magnetic fields. For every condition, pre-magnetised hMREs are able to absorb more energy before fracture than non-magnetised ones. For instance, the pre-magnetised sample with an initial length (l_0) of 30 mm and with a cut-width ratio (c/w) of 0.2 absorbs a 38 % more energy than the non-magnetised counterpart. For the cut-width ratios of 0.3, 0.4, and 0.5, the increases in the energy absorbed are 46, 49, and 16 %, respectively. Moreover, the work of extension for uncut samples is 0.0551 and 0.0982 mJ mm^{-3}, respectively for non-magnetised and pre-magnetised hMREs (see the results for the uncut case in Figure A.5). This gives an increase in the energy absorbed by pre-magnetised samples of 78 %. For the samples with initial length of 50 mm, the increases are 23, 51, 40, and 49 % for the same cut-width ratios. Overall, the pre-magnetised hMRE samples are tougher to fracture than non-magnetised ones.

A further finding relates to the size of the initial cut and the stretch to failure. The larger the flaw, the smaller the displacement to failure. For the cut-width ratios of 0.2, 0.3, 0.4, and 0.5 and initial length $l_0 = 30$ mm, the displacement to failure of non-magnetised samples is 51.9, 35.0, 34.4, and 31.4 mm, respectively. Chen and co-authors (Chen et al., 2017) elaborated on the dependency of the stretch to failure on the cut length of two stretch-stiffening highly stretchable elastomers: VHB and PU. For short cuts (i.e., below 0.1 mm length) the stretch to failure was in-

18

sensitive to the length of the cut. Similarly, for long cuts (i.e., above 10 mm) it barely depended on

335 the length. However, for intermediate lengths the dependency was maximum. Our results recover this tendency. For the largest cut ratios, the displacement to failure barely changes (35.0, 34.4, and 31.4 mm). For the smallest cut, the displacement to failure increases a 50 % (51.9 mm). Moreover, for an uncut sample, the displacement to failure increases to 100.5 mm (See Figure A.5). Note that the behaviour for cuts smaller than 2 mm was not explored due to the large manufacturing error

340 when applying small cuts in these sticky materials. Regarding the effect of the remanent magnetic fields, the results show that the stretch to failure barely depends on the pre-magnetisation state. Just for the cut-width ratio of 0.2 there is an apparent difference, wherein the stretch to failure for the pre-magnetised sample is larger than for the non-magnetised one. The larger manufacturing error explains such a discrepancy.

345

19
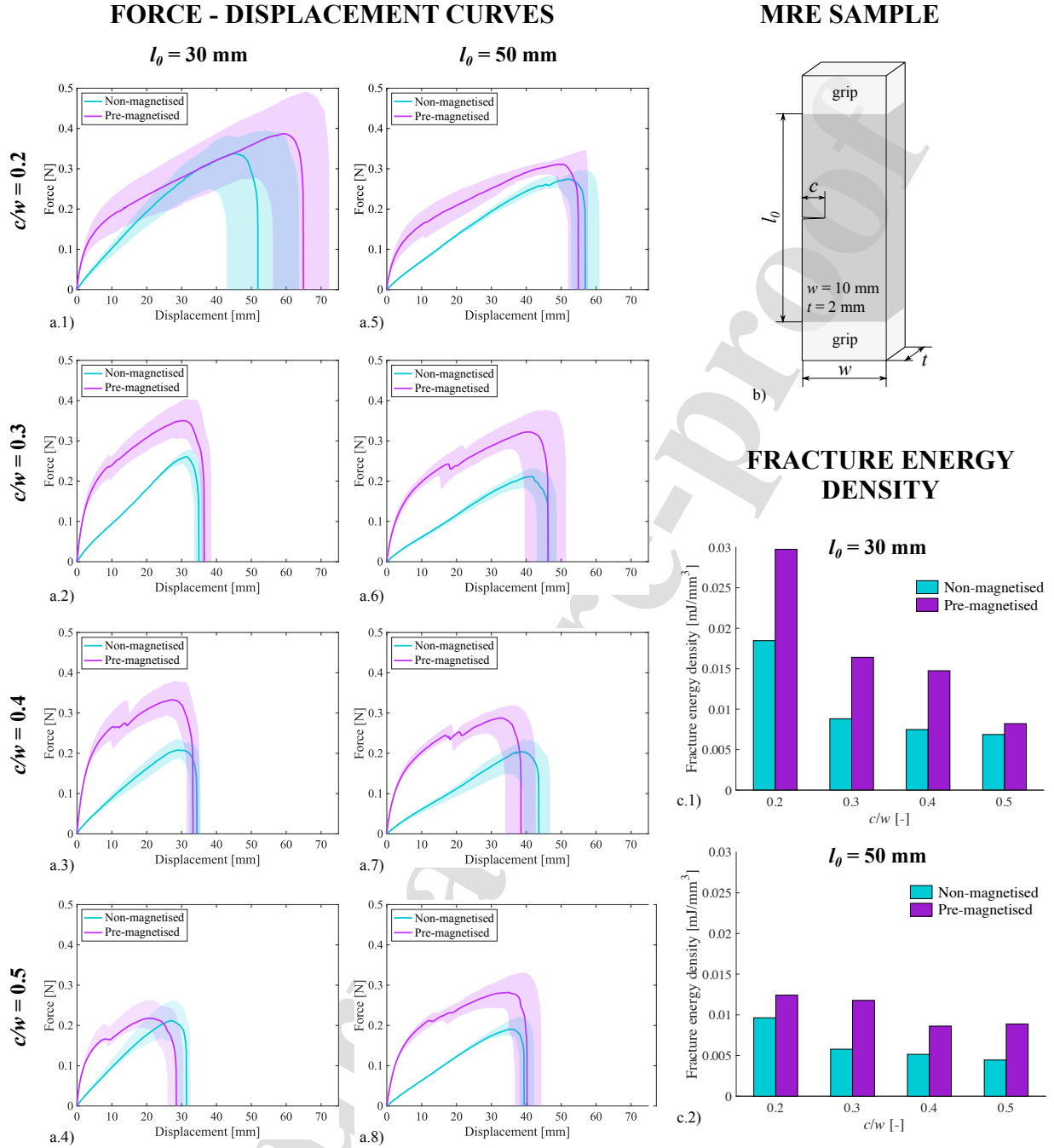
Figure 2. **Experimental results from tensile tests to rupture on non-magnetised and pre-magnetised samples and different pre-existing cuts.** (a.1-4) Results for the force-displacement curves, cut-width ratios c/w of 0.2, 0.3, 0.4, and 0.5 and initial length of the sample of 30 mm. (a.5-8) Results for the force-displacement curves for samples with initial length of 50 mm. Scatter areas around each mean curve are depicted to quantify the variability of experimental data sets. Three repetitions for each experimental condition ensure repeatability. (b) Illustration of the geometry of the sample, dimensions and position of the grips for the experimental procedure, with l_0 the initial distance between grips, t the depth of the sample and c the length of the pre-cut. The initial crack of length c is placed at the middle of the heigh. (c.1) Barplot with the fracture energy density of non-magnetised and pre-magnetised samples as a function of the cut length ratio for $l_0 = 30$ mm. (c.2) Barplot with the fracture energy density for $l_0 = 50$ mm.

20

3.2. Hard magnetics delay the opening of pre-existing cracks

Pre-magnetised hMREs behave as permanent magnets from a macroscopic point of view. Consequently, the free surfaces of a crack attract each other, thus closing the discontinuity. Under tensile loading, the interface provides structural support up to a certain axial load. Eventually, the crack opens when the mechanical stress in the bulk material becomes larger than the magnetic attraction. Figure 3.a provides pictures of the deformation process of a pre-magnetised hMRE sample during a tensile test. Three main stages characterise the process: i) the closed crack regime, ii) the crack opening phase, and iii) the eventual crack propagation. Note that the low stiffness of the matrix originates a blunt crack topology. In addition, the size of the magnetic fillers ($\sim 50\,\mu m$) is several orders smaller than the millimetric cracks, hence they do not mechanically interact with the crack tip. To provide a detailed study, we perform DIC on non-magnetised and pre-magnetised samples with different pre-existing cuts. The results consist in the surface displacement fields at the crack tip along quasi-static tensile tests.[6] More detail on the experimental procedure is provided in Methods 2.3.

For all tensile tests, two displacements are defined as control points: the first before the crack opens, i.e., "Displacement 1" of 10 mm, and the second after the opening of the crack, i.e., "Displacement 2" of 16 mm. Figure 3.d. illustrates the procedure and the closing mechanism. Furthermore, the reader can check a map of the magnetic induction around the crack tip in the pre-magnetised MRE in Appendix, Figure E.9. The results from the force-displacement curves in Figure 3.b show a drop in the force at the moment where the crack opens. In this regard, the longer the initial crack, the larger the drop in the force, with the maximum for the cut of 5 mm. Moreover, Figures 3.c.1-8 and 9-16 present the vertical strain fields at "Displacement 1" and "Displacement 2", respectively. A first finding relates to the small values of the strain on the crack tip for a closed

---

[6]The crack propagation is controlled in the quasi-static regime, thus preventing significant viscoelastic dissipation. Figure C.7 in Appendix provides additional results for cyclic loading and a faster velocity. In this regard, further efforts should address fast crack propagation and the underlying dissipative phenomena. Note that a thorough approach to rate-dependent mechanisms in MREs is experimentally and computationally provided in (Moreno et al., 2021; Lucarini et al., 2022).

370 crack (Figure 3.c.5-8). Indeed, when the crack has not yet opened the structural behaviour is close to that of a flawless sample. A second finding, after the opening of the crack (i.e., "Displacement 2"), is that strains at the crack tip are larger for pre-magnetised samples than for non-magnetised ones, see Figure 3c.13-16 and Figure 3c.9-12, respectively. Although the strain fields do not provide a complete view of the constitutive behaviour of the hMRE (i.e., stress response), they provide

375 a measure of the deformation state.

The J-integral provides a better quantification of the strain concentration at the crack tip. The estimation of this value is done with the analytical formulation of Long et al. (Long and Hui, 2015) for the crack tip fields under large deformations to fit the vertical displacement fields obtained with

380 DIC. The formulation is based on the Generalised neo-Hookean model (GNH). Moreover, the points used for the fitting are defined through an annular grid, see Figure 3.e.1. For further detail on the calibration of the model and the fitting procedure we refer to Methods 2.4. In addition, Figure B.6 contains additional results for alternative annular grids. This confirms that the fitting grid does not influence the tendencies found. Figure 3.e.2 shows the results for all cut-width ra-

385 tios, for "Displacement 1" and "Displacement 2" and for both non-magnetised and pre-magnetised samples. A first finding relates to the crack closure phenomenon. The values of J are significantly smaller for pre-magnetised samples than for non-magnetised hMREs at "Displacement 1". This result is explained by the crack closure due to remanent magnetic fields that provide material continuity through the crack region. The reduction is of approximately 11 %, 18 %, 23 %, and 23 %

390 for the crack length ratios of 0.2, 0.3, 0.4, and 0.5, respectively. However, once the crack opens in the pre-magnetised hMRE, J is larger for the pre-magnetised sample than for the non-magnetised one. It is 8.6 %, 9.4 %, 7.7 %, and 28 % larger, respectively for the crack length ratios.

An additional finding unveils that J shows a peak for cuts of intermediate lengths and, for short

395 and long cracks, J is smaller. In other words, the shortest and longest cracks (2 mm and 5 mm, respectively) lead to smaller strain concentration at the crack tip. However, for the intermediate cut-width ratio of $c/w = 0.3$, increases between 35 % and 60 % with respect to the case for the

22

shortest crack are shown in Figure 3.e.2. The smaller sensitivity of the hMRE to small flaws agrees
with the work conducted by Chen and co-authors (Chen et al., 2017). Regarding the large cuts, the
400 smaller J would owe to a more homogeneous displacement field at the crack tip. Overall, although
the experimental displacement fields can provide meaningful information, they miss constitutive
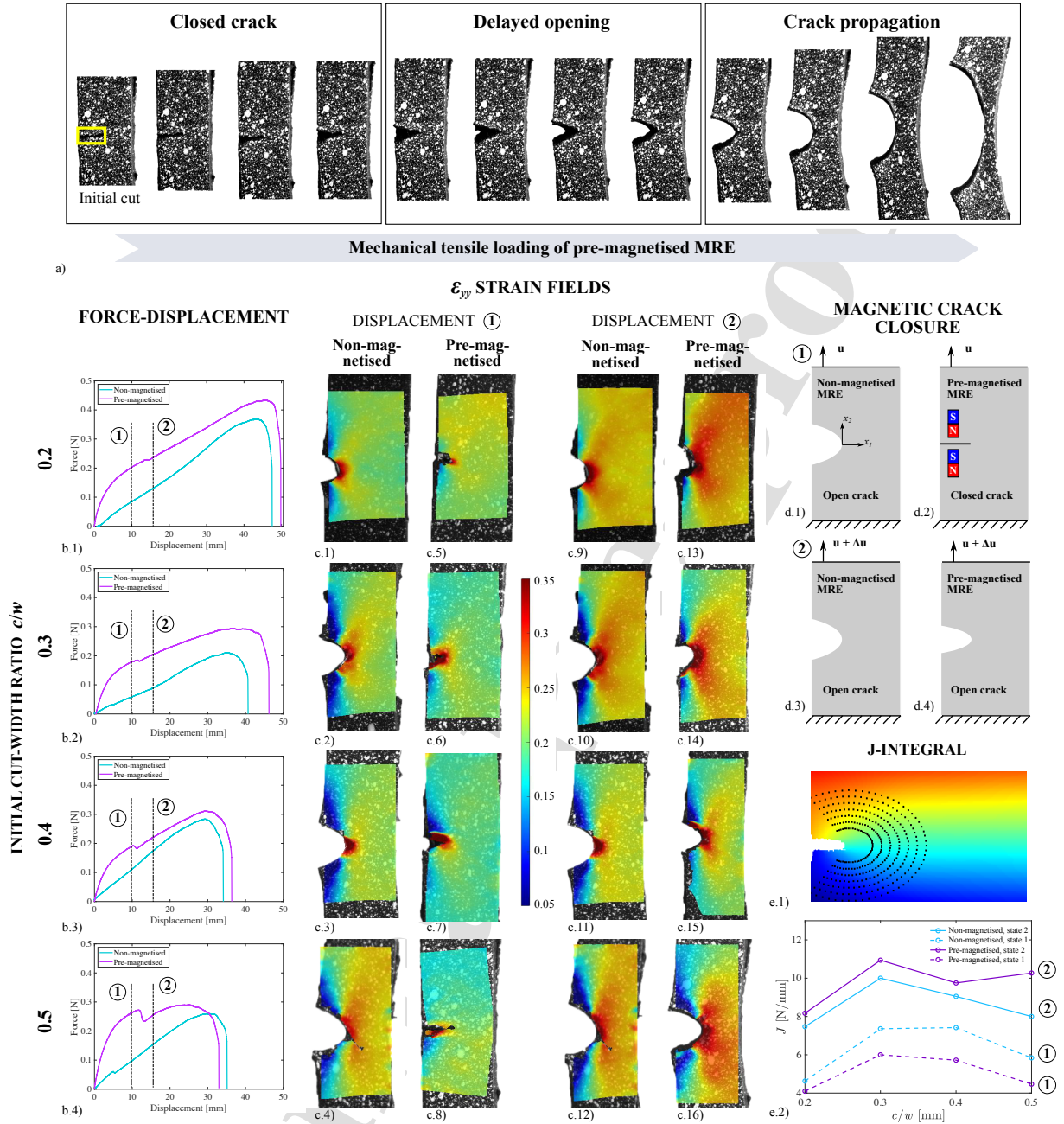information. Such additional information could be better considered through computational full-
field models.

Figure 3. Experimental results for the surface deformation at the crack tip on non-magnetised and pre-magnetised samples show the delay in the opening of the pre-existing crack. (a) Stages along the stretching of a pre-magnetised hMRE with a 5 mm crack. (b.1-4) Force-displacement curves for non-magnetised and pre-magnetised hMREs with pre-existing cut-width ratios of 0.2, 0.3, 0.4, and 0.5. Two displacements (abscissa) are defined: "Displacement 1", equal to 10 mm, is defined for all the samples before the opening of the crack in the pre-magnetised samples; and "Displacement 2", equal to 16 mm, after the crack opening. In between these two reference displacements, and for pre-magnetised samples, the sides of the crack detach. (c.1-4) and (c.5-8) Vertical strain fields at "Displacement 1" of non-magnetised and pre-magnetised samples, respectively. (c.9-12) and (c.13-16) Vertical strain fields at "Displacement 2" of non-magnetised and pre-magnetised samples, respectively. (d.1-2) and (d.3-4) Illustration of the crack state (open/closed) of non-magnetised and pre-magnetised state for Displacements 1 and 2, respectively. (e.1) Annular grid used for the fitting with the experimental and theoretical vertical displacement fields to estimate the J-integral. (e.2) Values of J for the non-magnetised and pre-magnetised samples at Displacements 1 and 2 as a function of the crack-width ratio.

3.3. Hard magnetics reduce stress concentration at the crack tip

The stress state at the crack tip drives crack growth. Given the complexity of the coupling between the mechanical and magnetic fields within pre-magnetised hMREs, experimental techniques are not enough to fully understand the constitutive response of hMREs. In this regard, DIC provides the displacement and strain fields of the deformed sample, but not the stress response. The highly complex behaviour of hMREs requires constitutive models that consider the interactions between the magnetic particles and the soft elastomeric matrix. Such approaches, when implemented in a computational framework, provide deeper understanding of the underlying physics.

In the present work, we develop a bespoke magneto-mechanical phase-field model to provide understanding on how remanent magnetic fields affect fracture mechanics of ultra-soft hMREs. More specifically, the framework explains the capacity of pre-magnetised hMREs to absorb more energy than non-magnetised ones, as reported in the previous sections. The model is based on a continuum description of the hMRE within the finite strain framework (Pelteret and Steinmann, 2020; Mukherjee et al., 2020; Mukherjee and Danas, 2022; Rambausek et al., 2022). The Generalised neo-Hookean model (GNH) is used to model the mechanical mechanical behaviour (Long and Hui, 2015) (see Eq. 25). Moreover, when the medium has remanent magnetisation and/or is externally actuated, the coupling between the magnetic and mechanical fields modulates the overall stress in the bulk material. To properly model the interaction between magnetic particles at the microscale, an additional coupling term is added to the magnetic formulation. Furthermore, the air (free space) surrounding the hMRE is modelled as an extremely compliant mechanical medium (Moreno-Mateos et al., 2022b; Pelteret et al., 2016). On top of this, an order parameter field models the damage of the medium and crack propagation. The calibration of the critical energy release rate G_c is achieved from experimental force-displacement rupture curves for cracks of 2 and 5 mm. The area between both curves provides G_c, see Figure 4.a. Note that this is an average estimation from the shortest crack to the largest one. The reader can find more detail on the calibration of the GNH model parameters in Appendix A.

25

We perform simulations for different magnetic remanent fields, i.e., $\mu_0\mathbb{H}_r = 0, 5, 10, 15, 20$ mT and the cut-width ratios $c/w = 0.2, 0.3, 0.4, 0.5$. Figure 4.b illustrates the morphology of the crack during its propagation in non-magnetised and pre-magnetised hMREs, from the 2 mm initial cut

435 to the eventual rupture of the sample. Force-displacement curves in Figure 4.c show increasing stiffness and stretch to failure for shorter cracks and larger remanent fields. Moreover, they allow to calculate the fracture energy from the area under the curve. In this regard, the barplots in Figure 4.d present the values of the fracture energy density, with increases of the fracture toughness above 50 % for the maximum 20 mT remanent field. Finally, Figure 4.e provides the vertical

440 Cauchy stress fields (σ_{yy}) near the crack tip for non-magnetised and pre-magnetised hMREs. For the pre-magnetised case, the stress concentration is smaller than for the non-magnetised hMRE. This is a consequence of the coupled response of the hMRE, that results from a mechanical balance between the polymeric network deformation and magnetic stresses from particle dipole-to-dipole interactions. An isolated study of the magnetic stress contribution indicates that the magnetic

445 stresses induce compression of the medium. In this regard, Figure D.8 depicts the distribution of the spherical component of the magnetic contribution to the Cauchy stress tensor, where the positive values indicate magnetic compression of the medium.
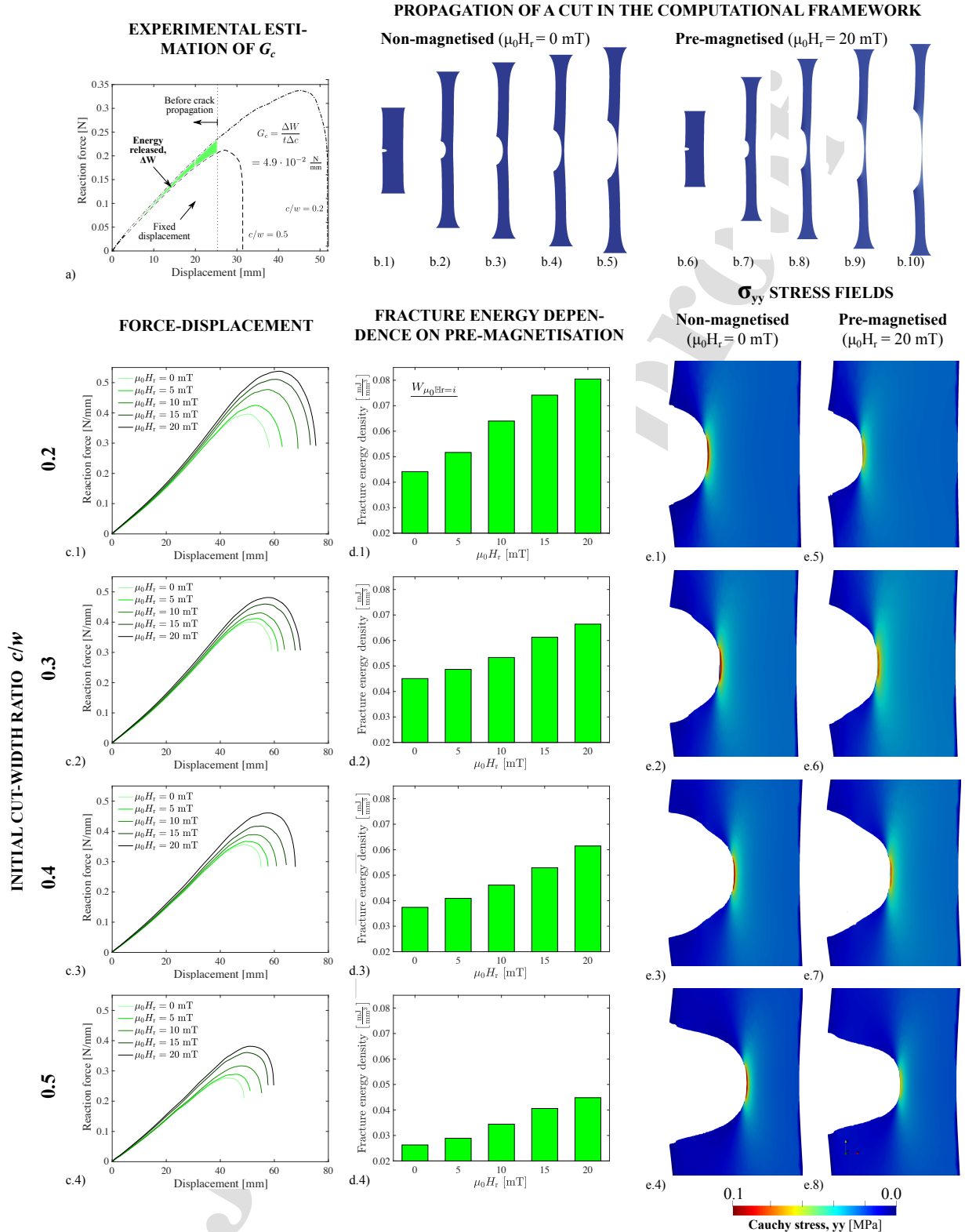
26

EXPERIMENTAL ESTIMATION OF G_c

PROPAGATION OF A CUT IN THE COMPUTATIONAL FRAMEWORK

Non-magnetised ($\mu_0 H_r = 0$ mT)   Pre-magnetised ($\mu_0 H_r = 20$ mT)

b.1) b.2) b.3) b.4) b.5)   b.6) b.7) b.8) b.9) b.10)

σ_{yy} STRESS FIELDS

FORCE-DISPLACEMENT   **FRACTURE ENERGY DEPENDENCE ON PRE-MAGNETISATION**   Non-magnetised ($\mu_0 H_r = 0$ mT)   Pre-magnetised ($\mu_0 H_r = 20$ mT)

INITIAL CUT-WIDTH RATIO c/w

Figure 4. **Numerical results from tensile tests to rupture performed in the virtual framework.** (a) Experimental calculation of the critical energy release rate to be used in the phase-field model. To provide an average estimation, it is calculated as the energy released between 2 mm and 5 mm cracks at a displacement of 25 mm. (b.1-5) Evolution of the morphology of the crack from an initial cut of 2 mm to final rupture of a non-magnetised hMRE. The pictures correspond to deformed states for displacements of the edges of 3, 36, 53, 60, and 64 mm. (b.6-10) Crack patterns from an initial cut of 2 mm to final rupture of a pre-magnetised hMRE. The pictures correspond to deformed states for displacements of 5, 25, 35, 46, and 54 mm. The dimensions of the virtual samples are 10 mm width and 30 mm height. (c.1-4) Force-displacement curves to rupture of rectangular hMRE specimens with initial crack-width ratios of 0.2, 0.3, 0.4, and 0.5, respectively, and remanent magnetic fields $\mu_0 \mathbb{H}_r = 0, 5, 10, 20$ mT. (d.1-4) Fracture energy density for the cut length ratios and remanent magnetic fields $\mu_0 \mathbb{H}_r = 0, 5, 10, 20$ mT. (e.1-4) and (e.5-8) Crack tip Cauchy vertical stress fields for non-magnetised ($\mu_0 \mathbb{H}_r = 0$ mT) and pre-magnetised samples ($\mu_0 \mathbb{H}_r = 20$ mT). All pictures correspond to a displacement of 11.5 mm. Note that the fracture contours are obtained for $d < 0.85$, so that the regions of negligible stress contribution are not displayed.

4. Discussion

The experimental and computational study indicates that remanent magnetization in ultra-soft hMREs enhances their fracture performance. Our experimental approach demonstrates that pre-magnetised hMRE samples are tougher to fracture than non-magnetised ones. In addition, we report crack closure due to a magnetic field as a phenomenon that delays the opening of cracks. The magnetic attraction between both sides of the crack acts as an artificial glue that heals the flaw. This ground-breaking capability suggests the application of pre-magnetised hMREs on smart structures less sensitive to pre-existing flaws and even on self-healing structures (Garcia-Gonzalez et al., 2023; Yimyai et al., 2022). Furthermore, these ultra-soft structures would have the features to modify their mechanical properties and perform functional shape changes under external magnetic actuation. A comprehensive computational framework based on a bespoke phase-field approach allows to better understand how the magneto-mechanical coupling affects crack propagation. The virtual testbed, based on the constitutive description of hMREs at finite strains and magneto-mechanical coupling, allows to compare between magnetic conditions and pre-existing cuts of different lengths.

The concentration of the displacement, strain and stress fields at the crack tip is affected by the length of the pre-existing cut and permanent magnetisation state. In this regard, the experimental strains at the crack tip in Figure 3.c are larger for pre-magnetised samples than for non-magnetised ones. Moreover, according to the results for J, the fields are larger for cuts of intermediate lengths. However, strain fields are not enough to properly understand the constitutive behaviour. Fracture mechanics is determined by the energy of the material and not only the strains. In this sense, the response of the material is given by a pure mechanical contribution and a magnetic one. The former can be determined from the deformation of the material. The latter, however, actuates as a pre-stress and cannot be determined experimentally. In this respect, the computational framework provides more insightful information based on the intricate magneto-mechanical coupling of the medium. The framework allows for a detailed study of the stress response, which drives crack propagation, and reveals that the stress concentration at the crack tip is smaller for pre-magnetised

28

hMREs than for non-magnetised ones (see Figure 4.e). This justifies the slower crack growth rate observed from the virtual experiments on pre-magnetised hMREs and, overall, their enhanced fracture behaviour.

480

As mentioned earlier in Section 3.1, pre-magnetised samples show higher fracture toughness. The computational framework clarifies this behaviour. From the constitutive decomposition of the stress state into mechanical and magnetic contributions, one can verify that the magnetic stress contribution induces compressive deformation of the medium. The positive spherical component

485 of the magnetic stress in Figure D.8 quantifies this tendency. It unravels larger magnetic compression in front of the crack tip, a result that suggests that the magnetic fields homogenise the stress distribution within the medium. This is a consequence of the coupled response of the hMRE, that results from a mechanical balance between the polymeric network deformation and magnetic stresses from the particles' dipole-dipole interactions. The findings indicate that the particles' in-

490 teractions oppose the elongation of the medium, hence increasing the fracture toughness of the hMRE. This would enable the design of structures with more complex geometries, diminishing the negative effect of stress concentrations around pre-existing flaws.

Overall, the experimental and computational evidence unveils that the magneto-mechanical

495 coupling provided by hard magnetics enhance the fracture behavior of hMREs in an autonomous way. This feature opens doors to the design of self sufficient functional structures that can undergo large deformations minimising fracture failure limitations. For example, skin patches based on soft polymers (Theocharidis et al., 2022), meshes for wound closure (Gao et al., 2021) and bioadhesive skin sensors (Wang et al., 2022a). Moreover, the crack closure mechanism on pre-magnetised

500 hMRE samples suggests the application of hMREs as a robust option to minimise fracture propensity. Here, the delay in the opening of the crack would reduce the amplitude of J during a load cycle, thus providing a better performance of hMREs under cyclic loading. The study of fatigue failure is out of the scope of this work, but the reader can consult the works by Sanoja et al. (Sanoja et al., 2021) and Li et al. (Li et al., 2020) for further experimental considerations, the work by Loew

29

505 et al. (Loew et al., 2020) and Alessi et al. (Alessi et al., 2018) for a computational approach, and the work of Zheng et al. (Zheng et al., 2022) for fatigue on hydrogels. Additional further work could focus on the computational study of crack nucleation and propagation from a microstructural viewpoint (Nguyen et al., 2015; Kumar and Lopez-Pamies, 2020), e.g., via computational homogenisation approaches. Furthermore, data-driven modelling could be a useful approach to

510 account for unintended flaws resulting from actual manufacturing processes (Carrara et al., 2021). Finally, as reported in a recent work by the authors (Moreno-Mateos et al., 2022b), the combination of soft-magnetic and hard-magnetic particles within the same elastomeric matrix could additionally improve the fracture behaviour of hMREs. Here, the soft-magnetic particles would create magnetic bridges around the hard-magnetic ones, enhancing the magneto-mechanical coupling.

Author contributions

All authors conceived the experimental and computational research. M.A.M.M. performed the experimental work and implemented the computational model. M.A.M.M. wrote the original manuscript. M.A.M.M. and D.G.G. conducted the formal analysis. All authors discussed the results and reviewed the paper.

Data availability

The data generated during the current study is available from the corresponding author upon reasonable request.

Code availability

The code generated during the current study is available from the corresponding author upon reasonable request.

Competing interests

The Authors declare no Competing Financial or Non-Financial Interests.

Appendix A. Calibration of the Generalised neo-Hookean model with uncut samples

Tensile tests on uncut samples allowed the calibration of the mechanical material parameters. The parameter b was set to 1 to mimic at small strains a neo-Hookean material. Then, the shear modulus G and exponent n are obtained for non-magnetised and for pre-magnetised hMREs by fitting the curve from the numerical model with the experimental ones. The mechanical contribution in the numerical model is calibrated from experimental results for tensile tests on non-magnetised samples (blue curves in Figure A.5.a) and the magnetic fields for the pre-magnetisation condition are included through a magnetic constitutive extension of the model. However, for the estimation of the J-integral on pre-magnetised specimens, the analytical GNH model is used without any magnetic extension, hence the GNH parameters are calibrated to include the magneto-rheological effect (purple curves in Figure A.5.a). Note that the fitting is done up to 1.4 logarithmic strain. Moreover, the barplot in Figure A.5.b presents the fracture energy density as a function of the cut-width ratio, including the uncut case.
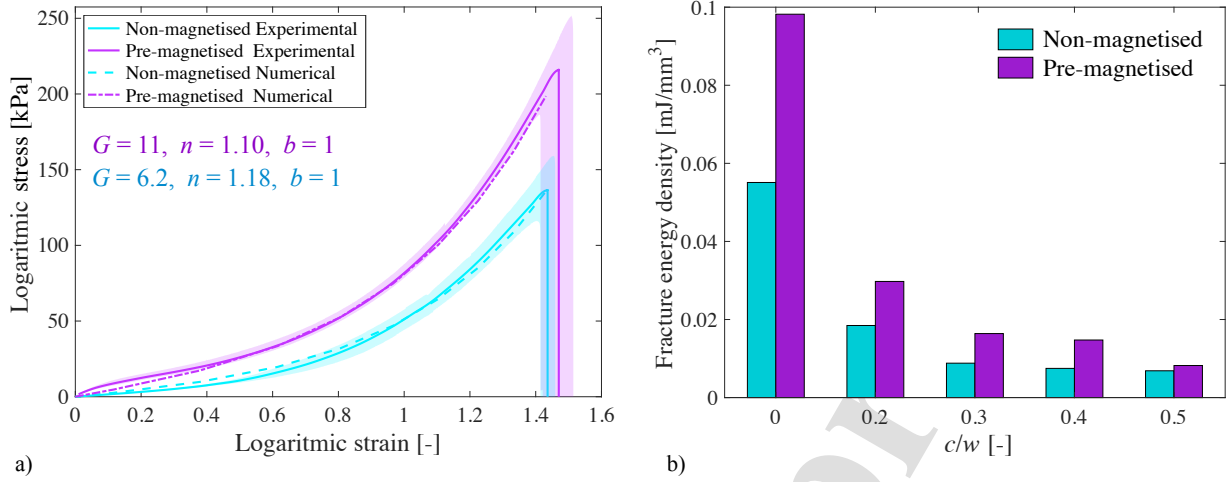
Figure A.5. **Results for the uncut samples case.** (a) Calibration of the material parameters of the Generalised neo-Hookean model with uniaxial tensile tests on uncut samples. Scatter areas around each mean curve are depicted to quantify the variability of experimental data sets. Three repetitions for each experimental condition ensure repeatability. A numerical model without damage field provides the numerical stress-strain curve as a function of the material parameters. These are fitted so that the numerical curve fits the experimental ones for uncut non-magnetised and pre-magnetised hMREs with initial length $l_0 = 30$ mm. (b) Barplot with the experimental fracture energy density of non-magnetised and pre-magnetised samples as a function of the cut length ratio for $l_0 = 30$ mm, including the results for the uncut case for initial length $l_0 = 30$ mm.

Appendix B. J-integral estimation for alternative annular grids

The annular grid used to fit the theoretical and experimental displacement fields must guarantee the fitting to be independent of the grid parameters. Here, we provide the results for J from two additional annular grids. The first grid has a smaller final angle; the second, a larger inner radius. The results follow the same tendencies as in Figure 2.e.2 regardless the grid parameters.
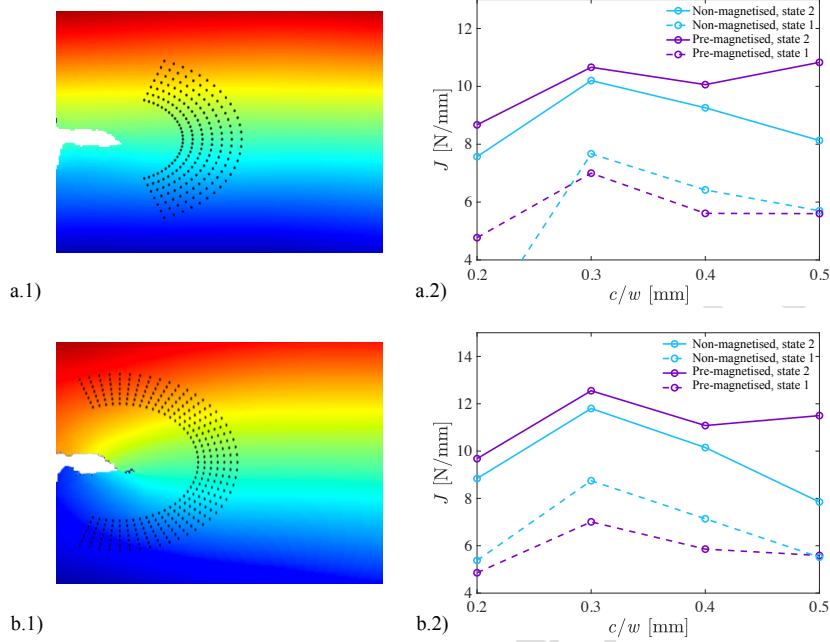
32

Figure B.6. **Results for the estimation of the J-integral for two different annular grids.** (a.1) Annular grid 1 with a smaller final angle and (b.1) annular grid 2 with a larger inner radius. (a.2), (b.2) Results for J-integral for the alternative fitting grids. The results prove the independence of J with the grid.

Appendix C. Inelastic behaviour of the hMRE for faster strain rates

Additional cyclic tensile tests to explore the hysteretic behaviour of the hMRE under tensile deformation. Two deformation velocities allow to explore the rate-dependent dissipation: the quasi-static velocity used in the work (0.003 mm s^{-1}) and a faster one (0.3 mm s^{-1}). In addition, the tests are performed on non-magnetised and pre-magnetised samples. These results demonstrate that, for the fracture tests performed, negligible dissipation occurs due to the mechanical viscous nature of the elastomeric matrix. However, higher rates will lead to such effects (Figure C.7.a). In addition, we performed the same experiments under pre-magnetised conditions. These results are interesting as a hysteresis response is observed even for the quasi-static case. Note that this problem is more complex due to magnetic stress contributions during the cyclic loading that result from the variation in particles' relative distances. We showed this latter effect numerically in a previous article (Lucarini et al., 2022).

33
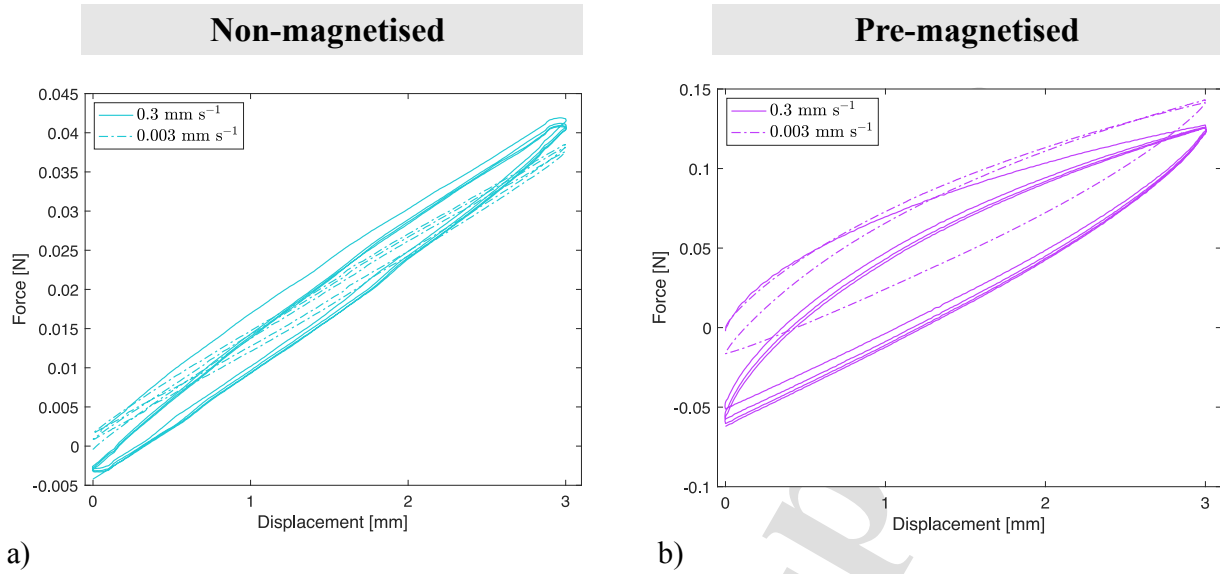
Non-magnetised

Pre-magnetised

a)

b)

Figure C.7. **Cyclic tests to explore the hysteretic behaviour of hMREs.** The experiments are conducted on: a) non-magnetised samples at loading rates of 0.3 mm s^{-1} and 0.003 mm s^{-1}; and b) pre-magnetised samples at loading rates of 0.3 mm s^{-1} and 0.003 mm s^{-1}.

Appendix D. Spherical component of the magnetic Cauchy stress tensor

The positive spherical component of the magnetic Cauchy stress tensor relates to a compressive stress contribution of the medium. Figure D.8 presents the results for different stages along the crack propagation on a virtual sample with initial notch of 2 mm.
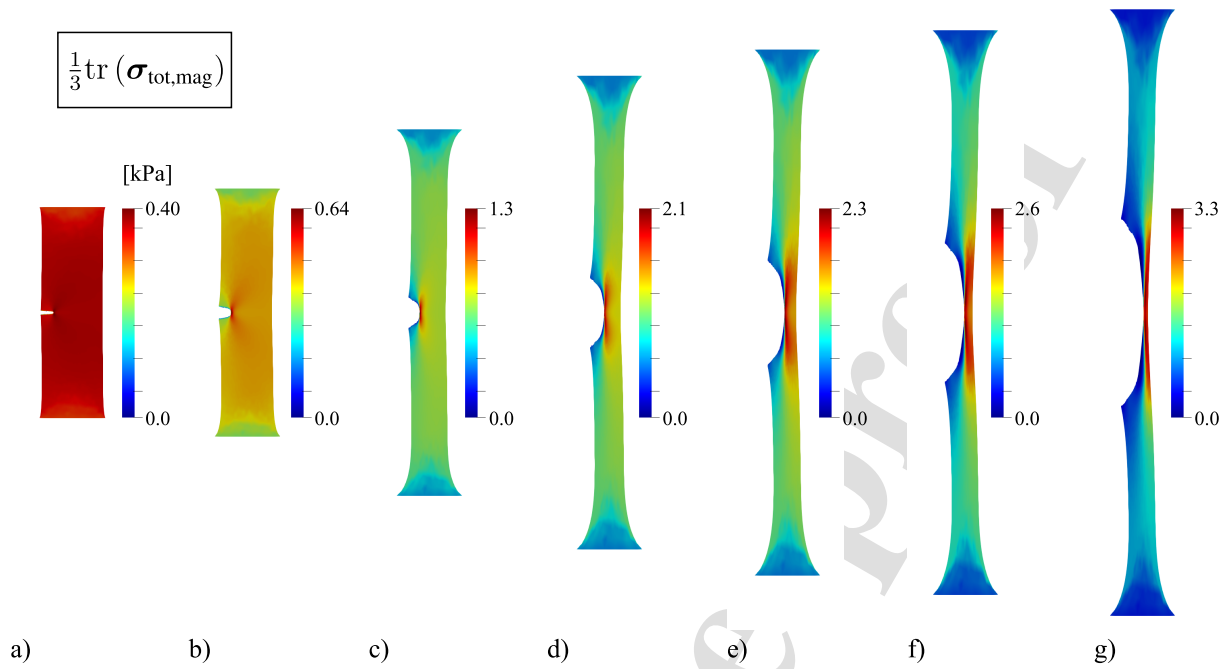
Figure D.8. **Spherical component of the magnetic Cauchy stress tensor along a virtual tensile test.** Positive values relate to a compressive deformation of the pre-magnetised MRE in the direction of the magnetic field. (a-g) Deformed configuration for displacements of 5, 25, 35, 46 and 54 mm, respectively.

Appendix E. Magnetic field in a pre-magnetised sample with a pre-cut

The vertical remanent magnetisation favours the crack closure and the opening originates heterogeneity in the magnetic field lines.
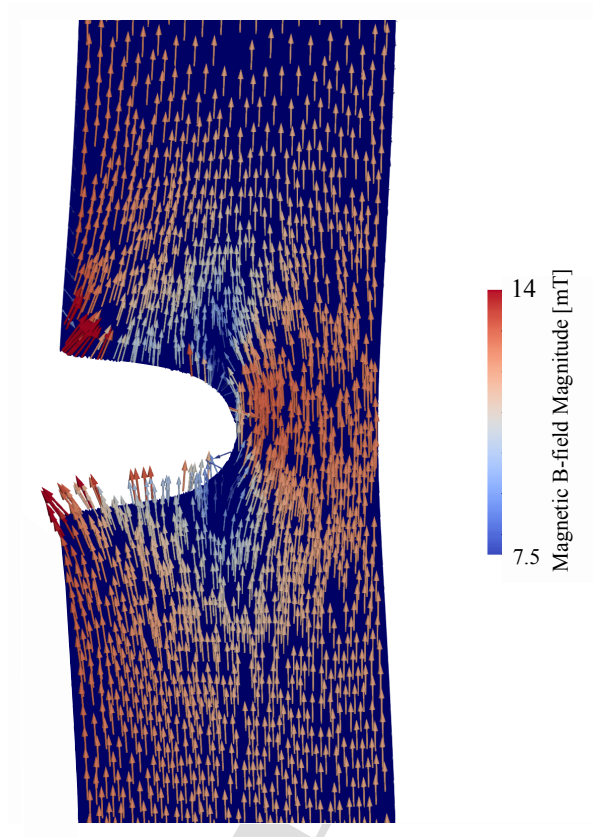
35

Figure E.9. **Magnetic induction in a pre-magnetised sample with a pre-cut.** The sample has a pre-existing crack of half the width of the sample. The opening of the crack originates heterogeneity in the magnetic field lines.

36

575 **References**

Ahmad, D., Patra, K., and Hossain, M. (2020). Experimental study and phenomenological modelling of flaw sensitivity of two polymers used as dielectric elastomers. *Continuum Mechanics and Thermodynamics*, 32:489–500.

Akono, A.-T., Reis, P. M., and Ulm, F.-J. (2011). Scratching as a fracture process: From butter to
580 steel. *Physical Review Letters*, 106:204302.

Alessi, R., Vidoli, S., and Lorenzis, L. D. (2018). A phenomenological approach to fatigue with a variational phase-field model: The one-dimensional case. *Engineering Fracture Mechanics*, 190:53–73.

Ambrosio, L. and Tortorelli, V. (1992). On the approximation of free discontinuity problems.
585 *Bollettino della Unione Matematica Italiana*, 6:105–123.

Bastola, A. K. and Hossain, M. (2021). The shape – morphing performance of magnetoactive soft materials. *Materials & Design*, 211:110172.

Begley, M. R., Creton, C., and McMeeking, R. M. (2015). The elastostatic plane strain mode i crack tip stress and displacement fields in a generalized linear neo-hookean elastomer. *Journal*
590 *of the Mechanics and Physics of Solids*, 84:21–38.

Carrara, P., Ortiz, M., and Lorenzis, L. D. (2021). Data-driven rate-dependent fracture mechanics. *Journal of the Mechanics and Physics of Solids*, 155:104559.

Chen, C., Wang, Z., and Suo, Z. (2017). Flaw sensitivity of highly stretchable materials. *Extreme Mechanics Letters*, 10:50–57.

595 Creton, C. and Ciccotti, M. (2016). Fracture and adhesion of soft materials: a review. *Reports on Progress in Physics*, 79:046601.

Gao, Y., Han, X., Chen, J., Pan, Y., Yang, M., Lu, L., Yang, J., Suo, Z., and Lu, T. (2021). Hydrogel–mesh composite for wound closure. *Proceedings of the National Academy of Sciences*, 118.

37

Garcia-Gonzalez, D., Moreno, M. A., Valencia, L., Arias, A., and Velasco, D. (2021). Influence of elastomeric matrix and particle volume fraction on the mechanical response of magneto-active polymers. *Composites Part B: Engineering*, 215:108796.

Garcia-Gonzalez, D., Ter-Yesayants, T., Moreno-Mateos, M. A., and Lopez-Donaire, M. L. (2023). Hard-magnetic phenomena enable autonomous self-healing elastomers. *Composites Part B: Engineering*, 248:110357.

Hirshikesh, Natarajan, S., Annabattula, R. K., and Martínez-Pañeda, E. (2019). Phase field modelling of crack propagation in functionally graded materials. *Composites Part B: Engineering*, 169:239–248.

Hu, W., Lum, G. Z., Mastrangeli, M., and Sitti, M. (2018). Small-scale soft-bodied robot with multimodal locomotion. *Nature*, 554:81–85.

Kalina, K. A., Brummund, J., Metsch, P., Kästner, M., Borin, D. Y., Linke, J. M., and Odenbach, S. (2017). Modeling of magnetic hystereses in soft mres filled with ndfeb particles. *Smart Materials and Structures*, 26:105019.

Kim, Y., Parada, G. A., Liu, S., and Zhao, X. (2019). Ferromagnetic soft continuum robots. *Science Robotics*, 4.

Kim, Y., Yuk, H., Zhao, R., Chester, S. A., and Zhao, X. (2018). *Printing ferromagnetic domains for untethered fast-transforming soft materials*, volume 558. Nature Publishing Group.

Kumar, A., Bourdin, B., Francfort, G. A., and Lopez-Pamies, O. (2020). Revisiting nucleation in the phase-field approach to brittle fracture. *Journal of the Mechanics and Physics of Solids*, 142:104027.

Kumar, A., Francfort, G. A., and Lopez-Pamies, O. (2018a). Fracture and healing of elastomers: A phase-transition theory and numerical implementation. *Journal of the Mechanics and Physics of Solids*, 112:523–551.

Kumar, A. and Lopez-Pamies, O. (2020). The phase-field approach to self-healable fracture of elastomers: A model accounting for fracture nucleation at large, with application to a class of conspicuous experiments. *Theoretical and Applied Fracture Mechanics*, 107:102550.

Kumar, A., Ravi-Chandar, K., and Lopez-Pamies, O. (2018b). The configurational-forces view of the nucleation and propagation of fracture and healing in elastomers as a phase transition. *International Journal of Fracture*, 213:1–16.

Lee, S. and Pharr, M. (2019). Sideways and stable crack propagation in a silicone elastomer. *Proceedings of the National Academy of Sciences*, 116:9251–9256.

Li, B. and Bouklas, N. (2020). A variational phase-field model for brittle fracture in polydisperse elastomer networks. *International Journal of Solids and Structures*, 182-183:193–204.

Li, C., Yang, H., Suo, Z., and Tang, J. (2020). Fatigue-resistant elastomers. *Journal of the Mechanics and Physics of Solids*, 134:103751.

Li, H., Wang, X., Hu, X., Xiong, J., Han, Q., Wang, X., and Guan, Z. (2021). Vibration and damping study of multifunctional grille composite sandwich plates with an imas design approach. *Composites Part B: Engineering*, 223:109078.

Li, R., Gou, X., Zhou, M., an Yang, P., Li, P., Shou, M., Liao, C., and Wang, X. (2022). Modeling and validation of multifield coupled self-sensing characteristics of magnetorheological elastomer for vibration isolators. *Materials & Design*, 217:110636.

Lin, S., Londono, C. D., Zheng, D., and Zhao, X. (2022). An extreme toughening mechanism for soft materials. *Soft Matter*, 18:5742–5749.

Lo, Y.-S., Hughes, T. J., and Landis, C. M. (2022). Phase-field fracture modeling for large structures. *Journal of the Mechanics and Physics of Solids*, page 105118.

Loew, P. J., Peters, B., and Beex, L. A. (2019). Rate-dependent phase-field damage modeling of rubber and its experimental parameter identification. *Journal of the Mechanics and Physics of Solids*, 127:266–294.

39

Loew, P. J., Peters, B., and Beex, L. A. (2020). Fatigue phase-field damage modeling of rubber using viscous dissipation: Crack nucleation and propagation. *Mechanics of Materials*, 142:103282.

Logg, A., Mardal, K.-A., and Wells, G., editors (2012). *Automated Solution of Differential Equations by the Finite Element Method*, volume 84. Springer Berlin Heidelberg.

Long, R. and Hui, C.-Y. (2015). Crack tip fields in soft elastic solids subjected to large quasi-static deformation — a review. *Extreme Mechanics Letters*, 4:131–155.

Long, R., Hui, C.-Y., Gong, J. P., and Bouchbinder, E. (2021). The fracture of highly deformable soft materials: A tale of two length scales. *Annual Review of Condensed Matter Physics*, 12:71–94.

Lopez-Donaire, M. L., de Aranda-Izuzquiza, G., Garzon-Hernandez, S., Crespo-Miguel, J., la Torre, M. F., Velasco, D., and Garcia-Gonzalez, D. (2022). Computationally guided diw technology to enable robust printing of inks with evolving rheological properties. *Advanced Materials Technologies*, page 2201707.

Lucarini, S., Moreno-Mateos, M. A., Danas, K., and Garcia-Gonzalez, D. (2022). Insights into the viscohyperelastic response of soft magnetorheological elastomers: Competition of macrostructural versus microstructural players. *International Journal of Solids and Structures*, 256:111981.

Ma, Z., Bourquard, C., Gao, Q., Jiang, S., Iure-Grimmel, T. D., Huo, R., Li, X., He, Z., Yang, Z., Yang, G., Wang, Y., Lam, E., hua Gao, Z., Supponen, O., and Li, J. (2022). Controlled tough bioadhesion mediated by ultrasound. *Science*, 377:751–755.

Miehe, C., Hofacker, M., and Welschinger, F. (2010a). A phase field model for rate-independent crack propagation: Robust algorithmic implementation based on operator splits. *Computer Methods in Applied Mechanics and Engineering*, 199:2765–2778.

Miehe, C. and Schänzel, L.-M. (2014). Phase field modeling of fracture in rubbery polymers. part i: Finite elasticity coupled with brittle failure. *Journal of the Mechanics and Physics of Solids*, 65:93–113.

40

Miehe, C., Welschinger, F., and Hofacker, M. (2010b). Thermodynamically consistent phase-field models of fracture: Variational principles and multi-field fe implementations. *International Journal for Numerical Methods in Engineering*, 83:1273–1311.

Moreno, M. A., Gonzalez-Rico, J., Lopez-Donaire, M. L., Arias, A., and Garcia-Gonzalez, D. (2021). New experimental insights into magneto-mechanical rate dependences of magnetorheological elastomers. *Composites Part B: Engineering*, 224:109148.

Moreno-Mateos, M. A., Gonzalez-Rico, J., Nunez-Sardinha, E., Gomez-Cruz, C., Lopez-Donaire, M. L., Lucarini, S., Arias, A., Muñoz-Barrutia, A., Velasco, D., and Garcia-Gonzalez, D. (2022a). Magneto-mechanical system to reproduce and quantify complex strain patterns in biological materials. *Applied Materials Today*, 27:101437.

Moreno-Mateos, M. A., Hossain, M., Steinmann, P., and Garcia-Gonzalez, D. (2022b). Hybrid magnetorheological elastomers enable versatile soft actuators. *npj Computational Materials*, 8:162.

Moreno-Mateos, M. A., Lopez-Donaire, M. L., Hossain, M., and Garcia-Gonzalez, D. (2022c). Effects of soft and hard magnetic particles on the mechanical performance of ultra-soft magnetorheological elastomers. *Smart Materials and Structures*, 31:065018.

Mukherjee, D., Bodelot, L., and Danas, K. (2020). Microstructurally-guided explicit continuum models for isotropic magnetorheological elastomers with iron particles. *International Journal of Non-Linear Mechanics*, 120:103380.

Mukherjee, D. and Danas, K. (2022). A unified dual modeling framework for soft and hard magnetorheological elastomers. *International Journal of Solids and Structures*, page 111513.

Mukherjee, D., Rambausek, M., and Danas, K. (2021). An explicit dissipative model for isotropic hard magnetorheological elastomers. *Journal of the Mechanics and Physics of Solids*, 151:104361.

Nguyen, T., Yvonnet, J., Zhu, Q.-Z., Bornert, M., and Chateau, C. (2015). A phase field method to simulate crack nucleation and propagation in strongly heterogeneous materials from direct imaging of their microstructure. *Engineering Fracture Mechanics*, 139:18–39.

Pathak, P., Arora, N., and Rudykh, S. (2022). Magnetoelastic instabilities in soft laminates with ferromagnetic hyperelastic phases. *International Journal of Mechanical Sciences*, 213:106862.

Pelteret, J.-P., Davydov, D., McBride, A., Vu, D. K., and Steinmann, P. (2016). Computational electro-elasticity and magneto-elasticity for quasi-incompressible media immersed in free space. *International Journal for Numerical Methods in Engineering*, 108:1307–1342.

Pelteret, J.-P. and Steinmann, P. (2020). *Magneto-Active Polymers: Fabrication, characterisation, modelling and simulation at the micro- and macro-scale*. De Gruyter.

Rambausek, M., Mukherjee, D., and Danas, K. (2022). A computational framework for magnetically hard and soft viscoelastic magnetorheological elastomers. *Computer Methods in Applied Mechanics and Engineering*, 391:114500.

Ren, Z., Hu, W., Dong, X., and Sitti, M. (2019). Multi-functional soft-bodied jellyfish-like swimming. *Nature Communications*, 10:2703.

Sanoja, G. E., Morelle, X. P., Comtet, J., Yeh, C. J., Ciccotti, M., and Creton, C. (2021). Why is mechanical fatigue different from toughness in elastomers? the role of damage by polymer chain scission. *Science Advances*, 7.

Schümann, M. and Odenbach, S. (2017). In-situ observation of the particle microstructure of magnetorheological elastomers in presence of mechanical strain and magnetic fields. *Journal of Magnetism and Magnetic Materials*, 441:88–92.

Silva, J., Gouveia, C., Dinis, G., Pinto, A., and Pereira, A. (2022). Giant magnetostriction in low-concentration magnetorheological elastomers. *Composites Part B: Engineering*, page 110125.

Sridhar, A. and Keip, M.-A. (2019). A phase-field model for anisotropic brittle fracturing of piezoelectric ceramics. *International Journal of Fracture*, 220:221–242.

Stepanov, G., Chertovich, A., and Kramarenko, E. (2012). Magnetorheological and deformation properties of magnetically controlled elastomers with hard magnetic filler. *Journal of Magnetism and Magnetic Materials*, 324:3448–3451.

Stephenson, R. A. (1982). The equilibrium field near the tip of a crack for finite plane strain of incompressible elastic materials. *Journal of Elasticity*, 12:65–99.

Swamynathan, S., Jobst, S., Kienle, D., and Keip, M.-A. (2022). Phase-field modeling of fracture in strain-hardening elastomers: Variational formulation, multiaxial experiments and validation. *Engineering Fracture Mechanics*, 265:108303.

Tan, Y., He, Y., and Li, X. (2022). Phase field fracture modeling of transversely isotropic piezoelectric material with anisotropic fracture toughness. *International Journal of Solids and Structures*, 248:111615.

Theocharidis, G., Yuk, H., Roh, H., Wang, L., Mezghani, I., Wu, J., Kafanas, A., Contreras, M., Sumpio, B., Li, Z., Wang, E., Chen, L., Guo, C. F., Jayaswal, N., Katopodi, X.-L., Kalavros, N., Nabzdyk, C. S., Vlachos, I. S., Veves, A., and Zhao, X. (2022). A strain-programmed patch for the healing of diabetic wounds. *Nature Biomedical Engineering*, pages 1–16.

Uslu, F. E., Davidson, C. D., Mailand, E., Bouklas, N., Baker, B. M., and Sakar, M. S. (2021). Engineered extracellular matrices with integrated wireless microactuators to study mechanobiology. *Advanced Materials*, 33:2102641.

Vasco-Olmo, J.M., Diaz, F.A., Garcia-Collado, A, and Dorado-Vicente R. (2015). Experimental evaluation of crack shielding during fatigue crack growth using digital image correlation. *Fatigue & Fracture of Engineering Materials & Structures*, 2:223-237

Vicentini, F., Carrara, P., and Lorenzis, L. D. (2023). Phase-field modeling of brittle fracture in heterogeneous bars. *European Journal of Mechanics - A/Solids*, 97:104826.

Wang, C., Chen, X., Wang, L., Makihata, M., Liu, H.-C., Zhou, T., and Zhao, X. (2022a). Bioadhesive ultrasound for long-term continuous imaging of diverse organs. *Science*, 377:517–523.

Wang, T., Ugurlu, H., Yan, Y., Li, M., Li, M., Wild, A.-M., Yildiz, E., Schneider, M., Sheehan, D., Hu, W., and Sitti, M. (2022b). Adaptive wireless millirobotic locomotion into distal vasculature. *Nature Communications*, 13:4465.

Wu, S., Hamel, C. M., Ze, Q., Yang, F., Qi, H. J., and Zhao, R. (2020). Evolutionary algorithm-guided voxel-encoding printing of functional hard-magnetic soft active materials. *Advanced Intelligent Systems*, 2:2000060.

Yimyai, T., Pena-Francesch, A., and Crespy, D. (2022). Transparent and self-healing elastomers for reconfigurable 3d materials. *Macromolecular Rapid Communications*, page 2200554.

Yu, Y., Landis, C. M., and Huang, R. (2020). Poroelastic effects on steady state crack growth in polymer gels under plane stress. *Mechanics of Materials*, 143:103320.

Zhang, Q. and Rudykh, S. (2022). Magneto-deformation and transverse elastic waves in hard-magnetic soft laminates. *Mechanics of Materials*, 169:104325.

Zhang, X., Chen, G., Fu, X., Wang, Y., and Zhao, Y. (2021). Magneto-responsive microneedle robots for intestinal macromolecule delivery. *Advanced Materials*, 33:2104932.

Zhao, J., Li, X., Tan, Y., Liu, X., Lu, T., and Shi, M. (2022). Smart adhesives via magnetic actuation. *Advanced Materials*, 34:2107748.

Zhao, R., Kim, Y., Chester, S. A., Sharma, P., and Zhao, X. (2019). Mechanics of hard-magnetic soft materials. *Journal of the Mechanics and Physics of Solids*, 124:244–263.

Zhao, X. (2017). Designing toughness and strength for soft materials. *Proceedings of the National Academy of Sciences*, 114:8138–8140.

Zheng, D., Lin, S., Ni, J., and Zhao, X. (2022). Fracture and fatigue of entangled and unentangled polymer networks. *Extreme Mechanics Letters*, 51:101608.

Zhou, Y., Hu, J., Zhao, P., Zhang, W., Suo, Z., and Lu, T. (2021). Flaw-sensitivity of a tough hydrogel under monotonic and cyclic loads. *Journal of the Mechanics and Physics of Solids*, 153:104483.

CRediT authorship contribution statement

All authors conceived the experimental and computational research. M.A.M.M. performed the experimental work and implemented the computational model. M.A.M.M. wrote the original manuscript. M.A.M.M. and D.G.G. conducted the formal analysis. All authors discussed the results and reviewed the paper.

Declaration of interests

☐ The authors declare that they have no known competing financial interests or personal relationships that could have appeared to influence the work reported in this paper.

☒ The authors declare the following financial interests/personal relationships which may be considered as potential competing interests:

Daniel Garcia-Gonzalez reports financial support was provided by European Research Council.

Daniel Garcia Gonzalez reports financial support was provided by Community of Madrid.

Miguel Angel Moreno-Mateos reports financial support was provided by Spain Ministry of Science

and Innovation. Sergio Lucarini, Kostas Danas and Miguel Angel Moreno-Mateos reports financial s

upport was provided by European Research Council.